

NASA TM



DECLASSIFIED-AUTHORITY MEMO.US:  
313. TAINE TO SPACE  
DATED JUNE 15, 1967

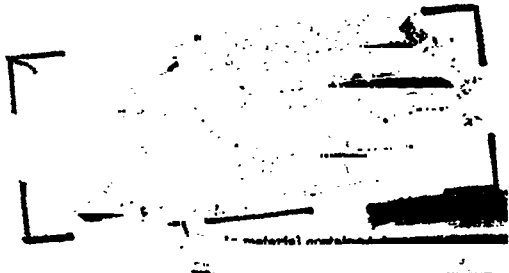
# TECHNICAL MEMORANDUM

## X-343

INVESTIGATION OF SOME EFFECTS OF FLEXIBILITY  
ON THE LIFT AND PITCHING-MOMENT CHARACTERISTICS OF A  
SERIES OF LOW-ASPECT-RATIO WING-BODY  
COMBINATIONS AT TRANSONIC SPEEDS

By Robert V. Doggett, Jr., and A. Gerald Rainey

Langley Research Center  
Langley Field, Va.



FACILITY FORM 602	447-32156	(THRU)
	(ACCESSION NUMBER)	
	50	(CODE)
	(PAGES)	
	X-343	81
	(NASA CR OR TMX OR AD NUMBER)	(CATEGORY)

NATIONAL AERONAUTICS AND SPACE ADMINISTRATION  
WASHINGTON

October 1960

[REDACTED]

NATIONAL AERONAUTICS AND SPACE ADMINISTRATION

TECHNICAL MEMORANDUM X-343

INVESTIGATION OF SOME EFFECTS OF FLEXIBILITY  
ON THE LIFT AND PITCHING-MOMENT CHARACTERISTICS OF A  
SERIES OF LOW-ASPECT-RATIO WING-BODY  
COMBINATIONS AT TRANSONIC SPEEDS\*

By Robert V. Doggett, Jr., and A. Gerald Rainey

Declassified by authority of NASA  
SUMMARY Classification Change Notices No. 113  
Dated \*\* 6/28/67

Measurements of lift and pitching moment were made on a series of low-aspect-ratio wing-body combinations of different stiffnesses in the Mach number range from 0.70 to 1.10 and at angles of attack up to  $30^\circ$ . The configurations tested consisted of three different delta wings in combination with a single conical-cylindrical body. The three delta wings differed in leading-edge-sweep angle, aspect ratio, and area. Both rigid and flexible models were tested at Reynolds numbers per foot of  $3.2 \times 10^6$  and  $1.8 \times 10^6$ .

The experimental results indicated that there is no appreciable effect of vehicle flexibility on the lift characteristics for the models tested. The pitching-moment characteristics were affected by flexibility; in general, increasing flexibility produced an appreciable deterioration of the static longitudinal stability characteristics.

Some of the experimental results were compared with some of the linear and nonlinear theoretical methods available. It is to be noted that in the theoretical calculations the models were assumed to consist only of a triangular wing, effects of the fuselage being ignored. The linear theory showed good agreement with the experimental results in values of the lift-curve slope at the zero-lift condition. One of the nonlinear theories showed fair agreement with the experimentally determined lift characteristics for all three configurations. None of the analytical methods used were completely adequate for the prediction of the lift and pitching-moment characteristics throughout the entire angle-of-attack range investigated.

---

\* Title, Unclassified.

[REDACTED]

## INTRODUCTION

The proposed use of low-aspect-ratio lifting vehicles for long-range hypersonic flight and for reentry into the earth's atmosphere has created a need for aerodynamic information to describe fully the behavior of such vehicles. One area where these vehicles have not received adequate attention consists of the aeroelastic problems of flutter, divergence, and deterioration of stability and control characteristics associated with elastic deformations. A preliminary study of these aeroelastic characteristics has indicated that this deterioration of stability and control characteristics might be very significant. Most proposed ascent trajectories for these vehicles produce relatively high dynamic pressures in the transonic speed range. Since aeroelastic effects tend to become more pronounced at conditions where the product of dynamic pressure and lift-curve slope is a maximum, it appeared desirable to study the lift and pitching-moment characteristics of a series of low-aspect-ratio wing-body configurations in this often troublesome speed regime.

Accordingly, a program has been completed in the Langley 2-foot transonic aeroelasticity tunnel where the lift and pitching moment have been measured on a series of full-span triangular-planform wing-body configurations varying in aspect ratio and stiffness. The measurements covered the Mach number range from 0.70 to 1.10 at angles of attack as high as  $30^\circ$ . The models were restrained at the trailing edge of the body by a balance which was attached to a conventional sting support system. The balance was shielded from the airstream by a fairing with a conical nose and cylindrical afterbody simulating a booster configuration. Thus, the lift and pitching-moment coefficients measured may be interpreted directly as representing the aerodynamic loads imposed on a booster by such a forward-mounted vehicle. Also of interest, however, are the implications contained in the data regarding the aeroelastic effects on the stability and control characteristics of free-flying vehicles of this type. The measured characteristics have been compared with those calculated by means of a relatively simple aeroelastic analysis.

## SYMBOLS

A	wing aspect ratio
$A_{ij}$	deflection influence coefficient (deflection at $i$ th point due to unit load at $j$ th point)
$\bar{c}$	wing mean aerodynamic chord

$c_r$	wing root chord
$C_L$	lift coefficient, $\frac{\text{Lift}}{qS}$
$C_{L_\alpha}$	lift-curve slope
$C_m$	pitching-moment coefficient, $\frac{\text{Pitching moment}}{qS\bar{c}}$
$C$	constant (see appendix)
$[D]$	differentiating matrix
$F$	aerodynamic force
$F_j$	aerodynamic force at $j$ th point
$i, j$	integers
$M$	Mach number
$q$	dynamic pressure
$s = x \tan \epsilon$	
$s_o$	wing semispan
$S$	wing planform area
$x, y, z$	Cartesian coordinates
$\Delta x$	element of width having its center at $x = x_j$
$x_{cp}$	distance from leading edge of mean aerodynamic chord to center of pressure measured in fraction of mean aerodynamic chord, positive rearward
$x_i$	distance from origin to $i$ th point
$x_j$	distance from origin to $j$ th point
$z_i$	deflection at $i$ th point due to flexibility
$z_j$	deflection at $j$ th point due to flexibility

$z'_j$	deflection at $j$ th point due to angle of attack
$\alpha$	angle of attack (measured at trailing edge of model)
$\alpha_c$	calculated angle of attack at station 1
$\alpha_e$	measured angle of attack at station 1
$\alpha_j$	rigid-body angle of attack at $j$ th point
$\delta_c$	calculated deflection at station 1
$\delta_e$	measured deflection at station 1
$\epsilon$	wing semiapex angle
$\lambda_{ij}$	lambda function, $\lambda_{ij} = 0$ when $i \neq j$ and $\lambda_{ij} = 1$ when $i = j$

Matrix notations:

$[ \ ]$	square
$\{ \}$	column

## APPARATUS AND TESTS

### Wind Tunnel

The Langley 2-foot transonic aeroelasticity tunnel was used in this investigation. This tunnel is a slotted-throat single-return wind tunnel equipped to use either air or Freon-12 as the test medium at pressures from 1 atmosphere down to about 1/25 atmosphere. The tunnel is of the continuous-operation type, powered by a motor-driven fan. Both test-section Mach number and density are continuously controllable. The present tests were made using Freon-12 as the test medium. Some of the characteristics of Freon-12 as a wind-tunnel test medium are discussed in reference 1.

### Models

Model description.- Three series of models were tested. Details of the geometry of the models are shown in figure 1. The configurations

[REDACTED]

tested consisted of three different low-aspect-ratio full-span delta wings in combination with a single conical-cylindrical body. Differences in the three series of wings were in leading-edge-sweep angle, aspect ratio, and area. The first series (hereinafter referred to as series A) had a sweep angle of  $78.03^\circ$  and an aspect ratio of 0.848. The second series (hereinafter referred to as series B) had a sweep angle of  $83.95^\circ$  and an aspect ratio of 0.424. The third series (hereinafter referred to as series C) had a sweep angle of  $78.03^\circ$  and an aspect ratio of 0.848; however, the wing area was one-half that of the models of series A. The differences between the models in any one series were in longitudinal bending stiffness. The individual models will be hereinafter designated by two letters, and, in some cases, a number will be added. The first letter will refer to the wing series; the second letter will differentiate between the rigid models (the letter "R" will be used) and the flexible models (the letter "F" will be used). There were two flexible models of the A series having different levels of stiffness which are distinguished by the designations AF-1 and AF-2. Model AF-2 is the more flexible model.

Model construction.- The models were constructed of aluminum, Paraplex, and a flexible plastic foam. The wings were molded from Paraplex. For the rigid models, the wings were impregnated with Fiberglass to increase the wing stiffness. The fuselage was molded from a lightweight flexible plastic foam. The fuselages for the flexible models were cut transversely at approximately 1-inch intervals to reduce the contribution of the fuselage stiffness to the total model stiffness. The cuts were covered with thin rubber sheet to preserve the aerodynamic contour and to prevent leakage. The primary contribution to the longitudinal bending stiffness of the models was provided by an aluminum-alloy spar which was bonded to the root chord of the wing. Variations of the stiffness were obtained by variations of the dimensions of the spar. Two transition strips of No. 60 carborundum grains were applied near the nose of the rigid models to simulate the roughness of the first two rubber-covered cuts on the flexible models. A photograph of a typical flexible model of series A with part of the fuselage removed is shown in figure 2.

Presented in table I is the measured deflection influence coefficient matrices for the flexible models tested. These coefficients are given as deflection in inches per pound for each of the 10 stations on the model shown in figure 3. Since the model was mounted on a strain-gage balance during the wind-tunnel tests, the influence coefficients were measured with the models mounted on the balance. It should be noted that the balance was relatively stiff. The flexibility of the balance may be conveniently expressed as a rotational spring constant. This constant was determined to be about 32,000 in-lb/radian with the effective axis of rotation located 2.064 inches rearward of the model

trailing edge. As an example of the effect of the balance on the overall flexibility of the model-balance system, the deflection at station 3 of model AF-1 due to a load at that point was increased by about 10 percent because of the balance flexibility. It should be noted that the rigid models were not infinitely stiff and perhaps would be more properly described as being very stiff in comparison with the flexible models.

Model support system.- The models were cantilever-mounted on a three-component strain-gage balance which was in turn attached to a support sting. A line drawing showing the planform of the model support system is shown in figure 4. The balance was shielded from the airstream by a conical-cylindrical fairing, the geometry of which is representative of the forward portion of a typical rocket booster system which would normally be attached to a full-scale vehicle. A line drawing of the fairing is shown in figure 5. A gap of approximately 1/16 inch was left between the trailing edge of the model and the balance shield. The sting support was attached to a circular turntable which formed part of the tunnel wall. By rotating the turntable the model angle of attack was varied. A photograph of a typical model mounted in the test section is shown in figure 6.

L  
6  
9  
4

#### INSTRUMENTATION AND DATA REDUCTION

The forces and moments acting on the models were measured by means of a three-component strain-gage balance. The normal-force, chord-force, and pitching-moment components of the balance were designed for maximum measurable loads of 120 pounds, 80 pounds, and 240 inch-pounds, respectively, with an accuracy of  $\pm 1/2$  percent of the maximum load.

At relatively small angles of attack the measured chord forces were small and, within the precision of the balances used, could not be determined with sufficient accuracy to justify their presentation. The pitching-moment measurements appeared to be affected by changes in the temperature of the balance. These effects caused some drift in the zero reading of the balance; however, since the calibration of the balance was essentially unaffected by temperature, the slope or shape of the pitching-moment curves were correct because all runs were made at essentially constant temperature.

All of the force and moment data have been reduced to coefficient form. The reference length and reference area used were the wing mean aerodynamic chord and the total wing area, respectively. The pitching-moment coefficient is referred to an axis on the surface of the wing, parallel to the wing trailing edge, and located at 42 percent of the mean aerodynamic chord. (See fig. 1.) The angle of attack  $\alpha$  is defined as the angle at the trailing edge.

## TEST CONDITIONS

The aerodynamic lift forces, drag forces, and pitching moments were determined at Mach numbers of 0.70, 0.80, 0.85, 0.90, 0.95, 1.00, 1.05, and 1.10 and at angles of attack from  $-4^\circ$  up to as high as  $30^\circ$ . All the models were tested at a Reynolds number per foot of approximately  $3.2 \times 10^6$ . Tests were also made on the models of series A at a Reynolds number per foot of approximately  $1.8 \times 10^6$ . Shown in figure 7 is the variation of the test-section dynamic pressure with Mach number for the two test Reynolds numbers. Since there were slight variations in the tunnel stagnation pressure between tests, the dynamic pressure at a given Mach number varied from run to run. The data in the figure give the maximum range covered for all runs. This variation in the tunnel stagnation pressure caused a maximum deviation in the Reynolds numbers of approximately 2 percent.

## EXPERIMENTAL RESULTS AND DISCUSSION

### Lift Data

Rigid models.- Presented in figure 8 is the variation of the lift coefficient with angle of attack for all the rigid models tested. In order to facilitate presentation of the data, staggered scales have been used in many of the figures and care should be taken in identifying the zero axis for each curve. In figure 8(a), data from tests on model AR at Reynolds numbers per foot of approximately  $3.2 \times 10^6$  and  $1.8 \times 10^6$  are presented. There appears to be no appreciable effect of Reynolds number on the variation of the lift coefficient with angle of attack for the rigid model of series A. Slight differences are noted in the data taken at the two Reynolds numbers, but these differences are within the experimental error. Consequently, in subsequent comparisons of lift data for the flexible models, the effects of Reynolds number are assumed to be negligible. Presented in figure 9 is a comparison of the lift-coefficient data for the rigid models of the three different configurations at several Mach numbers ( $M = 0.70, 0.90, 1.00, \text{ and } 1.10$ ). A general comparison of the data in figure 9 indicates that all the models show essentially the same type of variation of the lift coefficient with angle of attack.

Flexible models.- Presented in figure 10 is the variation of the lift coefficient with angle of attack for the flexible models tested. Also included in the figure are the faired curves from figure 8 for the rigid models. On comparing the data for the flexible models with that



for the rigid models, it is seen that the lift data are, for all practical purposes, unaffected by variations in model flexibility. It should be noted that the angle of attack is measured at the trailing edge.

#### Pitching-Moment Data

Rigid models.- Presented in figure 11 is the variation of the pitching-moment coefficient with lift coefficient for the rigid models tested. As is seen from figure 11(a), there are some differences in the data taken at the two Reynolds numbers for model AR. These differences may be associated with viscous effects; however, some of the difference may be attributed to inaccuracies in the experimental method or to the fact that the rigid model was not infinitely stiff. Since the tests at two Reynolds numbers involve two sets of values of dynamic pressure (shown in fig. 7), effects of deformation on the data may have been present. The general trend shown by the pitching-moment data for positive values of the lift coefficient is an almost linear decrease until some value of the lift coefficient, depending on the Mach number, is reached and then the pitching-moment data show an increase in value. The slope of the linear portion of this variation tends to become more negative with increasing Mach number.

Flexible models.- Presented in figure 12 is the variation of the pitching-moment coefficient with lift coefficient for the flexible models tested. An examination of these data shows that the trends are similar to those described for the rigid model.

A more direct indication of the effects of flexibility on the pitching-moment characteristics is given in figure 13 where the variation of pitching-moment coefficient with lift coefficient is shown for the models of the A series having three different stiffnesses. When the data are examined from the standpoint of the stability and control characteristics of a free-flying vehicle, several interesting aspects are noted. The rigid model would be stable about the chosen center-of-gravity axis at 42 percent of the mean aerodynamic chord for all Mach numbers. The rigid model indicates a pitchup instability at high lift coefficients for the lowest Mach number ( $M = 0.70$ ). At positive lift coefficients and at the lower Mach numbers, the models of increasing flexibility show a systematic decrease in the lift coefficient at which pitchup occurs. In addition, the most flexible model shows an unstable pitching-moment characteristic at negative lift coefficients for all Mach numbers. These rather serious effects of flexibility on the static longitudinal stability characteristics indicate that the aeroelastic characteristics of highly flexible vehicles of this type should be given careful consideration.

CONFIDENTIAL

9

## COMPARISONS WITH THEORY

### Lift Data

Several theories (refs. 2 to 8) are available for the prediction of the lift for low-aspect-ratio triangular wings. The theories of references 2 to 5 are developed for a rigid wing in a steady incompressible flow. In reference 6 a linear aerodynamic theory has been developed for a wing which can deform elastically in the camber direction. The theoretical method presented in reference 7 is similar to that of reference 6 but is more general since both steady and unsteady aerodynamic forces are considered. The subsonic lifting-surface theory presented in reference 8 has application to both the steady and unsteady case and also permits effects of model deformations on the aerodynamic forces to be taken into account.

The theory of reference 2 is based on the idealization of two-dimensional incompressible flow and gives for the lift coefficient at small angles of attack

$$C_L = \frac{\pi A \alpha}{2} \quad (\text{ref. 2}) \quad (1)$$

References 3 to 5 are extensions of the work of reference 2 to include nonlinear effects of viscosity. In these theories the expressions for the lift-force coefficient consist of a linear term (the result given by ref. 2) plus a nonlinear viscous term. However, by making slightly different assumptions as to the nature of the flow field in the vicinity of the wing, different expressions for the viscous term were determined. The expressions for the lift coefficients given by these references are

$$C_L = \frac{\pi A \alpha}{2} + \frac{A(\pi \alpha)^{3/2}}{4} \quad (\text{ref. 3}) \quad (2)$$

$$C_L = \frac{\pi A \alpha}{2} + \pi A^{1/3} \alpha^{5/3} \quad (\text{ref. 4}) \quad (3)$$

$$C_L = \frac{\pi A \alpha}{2} + \pi A^{1/3} \alpha^{5/3} \left[ 1 + \frac{2}{3} \left( \frac{\alpha}{A} \right)^{2/3} \right] \quad (\text{ref. 5}) \quad (4)$$

It is to be noted that all calculations were made by considering the models to consist only of a triangular wing, effects of the fuselage

being ignored. A comparison of the experimentally determined lift coefficients for the rigid models tested with the theoretical values obtained from equations (1) to (4) is presented in figure 14. Only experimental data for  $M = 0.70$  are included in the figure since these data are typical of all data obtained. Also included in figure 14(a) are the results obtained by using a subsonic lifting-surface treatment. This method is developed in reference 8 for the unsteady case by using a spanwise numerical integration of the kernel function of unsteady, three-dimensional compressible flow. By considering the case where the reduced frequency equals zero, results for steady flow are obtained. The curve presented has been calculated for  $M = 0.70$ . As is seen from figure 14(a), none of the theories are satisfactory for predicting the variation of the lift coefficient with angle of attack throughout the entire range of angle of attack for the models of series A and C. At low angles of attack, the linear theory and the lifting-surface theory (refs. 2 and 8) show the best agreement with the experimental data. At higher angles of attack ( $\alpha > 10^\circ$ ), the theory of reference 3 gives the best prediction for model AR and the lifting-surface theory (ref. 8) gives the best prediction for model CR. In figure 14(b) the theory of reference 3 satisfactorily predicts the variation of the lift coefficient with angle of attack for model BR throughout the entire angle-of-attack range.

Presented in figure 15 is the variation with Mach number of the experimental lift-curve slope at the zero-lift condition for the models of all three series. The experimental values were determined by numerically differentiating the experimental lift data with a five-point differentiating scheme. Also included in the figure are the corresponding theoretical values obtained from the theory of reference 2. Included in figure 15(a) is the calculated lift-curve slope obtained by the method of reference 8. As is seen from the figure, the results obtained from the linear low-aspect-ratio aerodynamic theory are in good agreement with the experimental data. The three-dimensional theory of reference 8 predicts a value of the lift-curve slope somewhat higher than the value found experimentally.

It is observed that the usual relatively large deviations in lift-curve slope found for most configurations in the transonic speed range were not encountered in these tests. This is believed to be due to the slenderness of the configurations tested. It is of interest that the theory of reference 8, which takes account of Mach number, also shows the same trend as the experiments.

In reference 6 linear low-aspect-ratio aerodynamic theory has been applied to a low-aspect-ratio triangular wing which is allowed to deform elastically in the camber direction. The total lift force was found to be independent of the deformations and dependent only on the slope at the trailing edge. Thus the lift on the flexible wing at a given angle

of attack, measured at its trailing edge, would be the same as the lift on a rigid wing. Apparently, the increased lift generated by the higher local angles near the nose are compensated for by the negative lift forces associated with the curvature of the wing. Although linear theory is inadequate for the prediction of the magnitudes of the lift coefficient throughout the test angle-of-attack range, the experimental results are consistent with the results which would be expected from the method of reference 8 in that no appreciable effect of flexibility was found in the lift data. (See figs. 10 and 15.)

#### Center-of-Pressure Data

The location of the aerodynamic center of pressure as a fraction of mean aerodynamic chord for model AR is presented in figure 16. Also included is the center-of-pressure location as predicted by the theories of references 2 and 8. Both theories predict a more rearward location than was found experimentally. Both the experiment and the lifting-surface theory (ref. 8) show a rearward movement of the center of pressure with increasing Mach number.

#### Pitching-Moment Data

Figure 17 presents a comparison of some experimental and calculated variations of the pitching-moment coefficient with lift coefficient for the three series of models tested. Calculations were made for all the configurations by using the theory of reference 2. Calculations were also made for one of the flexible models of series A by using the linear low-aspect-ratio aerodynamic theory and allowing the model to deform elastically in the camber direction (ref. 7). The deformed shape used in this calculation is presented in figure 18. As is seen from figure 17(a), the calculations for the rigid model based on reference 2 do not satisfactorily predict the variation of the pitching-moment coefficient with lift coefficient for any of the three configurations. Of course, this linear theory could not be expected to predict the pitchup tendency at high lift coefficients. In addition, some of the discrepancy between theory and experiment may be due to the omission of the effects of the body in the calculation. In figure 17(b) it can be seen that the calculation for the flexible model shows much better agreement with experiment than did the calculations for the rigid models; however, the calculation for the flexible model cannot be considered to yield an adequate estimate of the pitching-moment characteristics.

### Elastic Deformations

A comparison of calculated and measured normalized shapes for model AF-1 is presented in figure 18. The type of deformed shape obtained on the flexible models was basically a bending in the camber direction. Some significant bending in the spanwise direction was also observed at high angles of attack. The experimental deflection shapes were determined by taking a double-exposure photograph of model AF-1 which had been painted black with very thin stripes of white running in the camber direction. One exposure was made with the wind off and the model at  $0^\circ$  angle of attack; whereas, the second exposure was taken at the desired test condition. By measuring the deflections of the white lines, the deformed shape of the model was determined. The calculated deflection shapes were determined by using a matrix iteration technique employing the linear low-aspect-ratio aerodynamic theory of reference 7 and measured deflection influence coefficients. This analysis is developed in detail in the appendix. The shapes presented in figure 18 have been normalized to the value of the deflection at station 1. (See fig. 3 for station 1 location.) The actual deflection at station 1 is indicated in figure 18. The values of both the calculated and measured angles of attack at station 1 are also tabulated in figure 18. It is seen in figure 18 that the general shapes of the experimental and theoretical curves compare favorably. However, the theory predicts a higher total deflection than was found experimentally.

As a matter of reference, the divergence dynamic pressures were calculated for all the flexible models tested by using a technique similar to that developed in reference 9. This technique is developed in the appendix. These values of the dynamic pressure were 2,822 lb/sq ft, 1,495 lb/sq ft, and 4,624 lb/sq ft for models AF-1, AF-2, and BF, respectively. At the maximum test conditions, models AF-1, AF-2, and BF were tested at approximately 9 percent, 17 percent, and 6 percent of their calculated divergence dynamic pressures, respectively.

### CONCLUDING REMARKS

Measurements of lift and pitching moment were made on a series of low-aspect-ratio wing-body combinations of different stiffnesses in the Mach number range from 0.70 to 1.10 and at angles of attack up to  $30^\circ$ . The configurations tested consisted of three different delta wings in combination with a single conical-cylindrical body. The three delta wings differed in leading-edge-sweep angle, aspect ratio, and area. Both rigid and flexible models were tested at Reynolds numbers per foot of  $3.2 \times 10^6$  and  $1.8 \times 10^6$ .

The experimental results indicated that there is no appreciable effect of vehicle flexibility on the lift characteristics for the models tested. The pitching-moment characteristics were affected by flexibility; in general, increasing flexibility produced an appreciable deterioration of the static longitudinal stability characteristics.

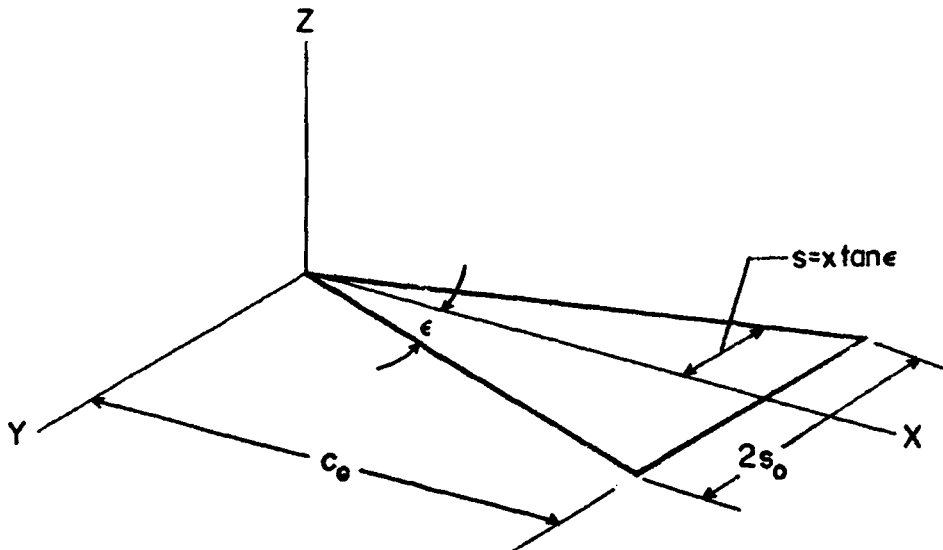
Some of the experimental results were compared with some of the linear and nonlinear theoretical methods available. It is to be noted that in the theoretical calculations the models were assumed to consist only of a triangular wing, effects of the fuselage being ignored. The linear theory showed good agreement with the experimental results in values of the lift-curve slope at the zero-lift condition. One of the nonlinear theories showed fair agreement with the experimentally determined lift characteristics for all three configurations. None of the analytical methods used were completely adequate for the prediction of the lift and pitching-moment characteristics throughout the entire angle-of-attack range.

Langley Research Center,  
National Aeronautics and Space Administration,  
Langley Field, Va., July 12, 1960.

## APPENDIX

## TECHNIQUE EMPLOYED IN CALCULATING DEFORMED SHAPES

A method of analysis was developed for calculating the deformed shapes of the flexible models by using the aerodynamic forces obtained from the theory presented in reference 7 for low-aspect-ratio triangular wings and measured deflection influence coefficients. The model is represented structurally and geometrically as shown in the following sketch:



The wing in its neutral position is assumed to have its mean camber surface lying in the XY-plane of the  $x, y, z$  coordinate system with the wing apex at the origin of the coordinate system and the root chord coinciding with the X-axis. The Z-axis is taken as positive upward, and a wind of constant velocity and inclination  $\alpha$  to the XY-plane emanates from the negative x-direction. The trailing edge of the wing is considered to be built in and the wing is allowed to only have deformations in the camber direction.

For any type of loading, the elastic deflection at any point  $x = x_1$  on the wing is defined by

$$z_1 = A_{11}F_1 + A_{12}F_2 + A_{13}F_3 \dots + A_{1j}F_j \quad (A1)$$

where  $A_{ij}$  is an elastic deflection influence coefficient defined as the deflection at position  $x = x_i$  due to a unit load at position  $x = x_j$ . For the present analysis the wing was divided into 10 chord-wise segments. Generalizing equation (A1) to include all the control points on the wing leads to the following deflection influence coefficient equation:

$$\{z_i\} = [A_{ij}] \{F_j\} \quad (A2)$$

For the case where  $\alpha = 0^\circ$ , the aerodynamic force per unit chord as given by reference 7 is

$$\frac{dF}{dx} = 2\pi q \tan^2 \epsilon \left( x^2 \frac{d^2 z}{dx^2} + 2x \frac{dz}{dx} \right) \quad (A3)$$

By considering an element of width  $\Delta x$  having its center at  $x = x_j$ , the total aerodynamic force on this element is given by

$$F_j = 2\pi(\Delta x)q \tan^2 \epsilon \left[ x_j^2 \left( \frac{d^2 z}{dx^2} \right)_j + 2x_j \left( \frac{dz}{dx} \right)_j \right] \quad (A4)$$

Rewriting equation (A4) in matrix notation for the entire wing gives the following equation:

$$\{F_j\} = 2\pi(\Delta x)q \tan^2 \epsilon \left\{ x_j^2 \left( \frac{d^2 z}{dx^2} \right)_j + 2x_j \left( \frac{dz}{dx} \right)_j \right\} \quad (A5)$$

With the use of the expressions  $\lambda_{ij} = 1$  when  $i = j$  and  $\lambda_{ij} = 0$  when  $i \neq j$ , equation (A5) can be rewritten in the form

$$\{F_j\} = 2\pi(\Delta x)q \tan^2 \epsilon \left\{ [\lambda_{ij} x_j^2] \left\{ \left( \frac{d^2 z}{dx^2} \right)_j \right\} + 2[\lambda_{ij} x_j] \left\{ \left( \frac{dz}{dx} \right)_j \right\} \right\} \quad (A6)$$



By determining a differentiating matrix  $[D]$  such that

$$\left\{ \left( \frac{d^2 z}{dx^2} \right)_j \right\} = [D] \left\{ \left( \frac{dz}{dx} \right)_j \right\} \quad (A7)$$

equation (A6) may be written in terms of slope only. The resulting equation is

$$\{F_j\} = 2\pi(\Delta x)q \tan^2 \epsilon \left[ [\lambda_{1j} x_j^2] [D] + 2[\lambda_{1j} x_j] \right] \left\{ \left( \frac{dz}{dx} \right)_j \right\} \quad (A8)$$

Since all of the premultipliers of the matrix  $\left\{ \left( \frac{dz}{dx} \right)_j \right\}$  in equation (A8) with the exception of  $q$  are constants peculiar to the particular configuration, the aerodynamic force may be expressed as

$$\{F_j\} = q[C] \left\{ \left( \frac{dz}{dx} \right)_j \right\} \quad (A9)$$

Again employing the differentiating matrix  $[D]$  such that

$$\left\{ \left( \frac{dz}{dx} \right)_j \right\} = [D] \{z_j\} \quad (A10)$$

the aerodynamic force becomes

$$\{F_j\} = q[C][D] \{z_j\} \quad (A11)$$

On substituting equation (A11) into the deflection influence coefficient equation (eq. (A2)), the final equation for the case  $\alpha = 0^\circ$  is obtained:

$$\{z_1\} = q[A_{1j}][C][D]\{z_j\} \quad (A12)$$

By iterating equation (A12) for the dominant root, the divergence dynamic pressure is obtained. This result is essentially the same as that presented in reference 9.

For the case  $\alpha \neq 0^\circ$ , there is an aerodynamic force associated with the angle of attack in addition to the force due to the elastic deformations. The force for the wing acting as a rigid body at an angle of attack may be expressed in matrix notation by the following equation:

$$\{F_j\} = 2\pi(\Delta x)q \tan^2 \epsilon \left[ 2[\lambda_{1j}x_j] \right] \{\alpha_j\} \quad (A13)$$

Since

$$[D]\{\alpha_j\} = 0$$

equation (A13) may be rewritten in the form of equation (A8)

$$\{F_j\} = 2\pi(\Delta x)q \tan^2 \epsilon \left[ [\lambda_{1j}x_j^2][D] + 2[\lambda_{1j}x_j] \right] \{\alpha_j\} \quad (A14)$$

with the use of the matrix  $[C]$  and the relationship

$$\{\alpha_j\} = [D]\{z'_j\}$$

equation (A14) becomes

$$\{F_j\} = q[C][D]\{z'_j\} \quad (A15)$$

By adding equations (A11) and (A15) and substituting the result into the deflection influence coefficient equation (eq. (A2)), the final equation for the case  $\alpha \neq 0$  is obtained:

$$\{z_1\} = q[A_{1j}][C][D]\{z_j + z'_j\} \quad (A16)$$

For the case  $\alpha = 0^\circ$  equation (A16) reduces to equation (A12). Equation (A16) is iterated for the deformed wing shape by using the desired initial angle of attack and dynamic pressure.

## REFERENCES

1. Von Doenhoff, Albert E., Braslow, Albert L., and Schwartzberg, Milton A.: Studies of the Use of Freon-12 as a Wind-Tunnel Testing Medium. NACA TN 3000, 1953.
2. Jones, Robert T.: Properties of Low-Aspect-Ratio Pointed Wings at Speeds Below and Above the Speed of Sound. NACA Rep. 835, 1946. (Supersedes NACA TN 1032.)
3. Küchemann, D.: A Non-Linear Lifting-Surface Theory for Wings of Small Aspect Ratio with Edge Separations. Rep. No. Aero 2540, British R.A.E., Apr. 1955.
4. Edwards, R. H.: Leading-Edge Separation From Delta Wings. Jour. Aero. Sci. (Readers' Forum), vol. 21, no. 2, Feb. 1954, pp. 134-135.
5. Brown, Clinton E., and Michael, William H., Jr.: On Slender Delta Wings With Leading-Edge Separation. NACA TN 3430, 1955.
6. Bisplinghoff, Raymond L., Ashley, Holt, and Halfman, Robert L.: Aeroelasticity. Addison-Wesley Pub. Co., Inc. (Cambridge, Mass.), c.1955, pp. 244-249.
7. Garrick, I. E.: Some Research on High-Speed Flutter. Third Anglo-American Aero. Conf., Sept. 4-7, 1951 (Brighton, England). R.A.S., 1952, pp. 419-446J.
8. Watkins, Charles E., Woolston, Donald S., and Cunningham, Herbert J.: A Systematic Kernel Function Procedure for Determining Aerodynamic Forces on Oscillating or Steady Finite Wings at Subsonic Speeds. NASA TR R-48, 1959.
9. Martin, Dennis J., and Watkins, Charles E.: Transonic and Supersonic Divergence Characteristics of Low-Aspect-Ratio Wings and Controls. Rep. No. 59-58, Inst. Aero. Sci., Jan. 1959.

TABLE I  
DEFLECTION INFLUENCE COEFFICIENT MATRICES  
(a) Model AF-1

$A_{ij}$ , in./lb, at -										
$j \backslash i$	1	2	3	4	5	6	7	8	9	10
1	0.1040	0.0756	0.0550	0.0395	0.0282	0.0179	0.0125	0.0067	0.0029	0.0016
2	.0756	.0613	.0468	.0342	.0247	.0158	.0110	.0060	.0027	.0015
3	.0550	.0468	.0388	.0289	.0212	.0137	.0095	.0053	.0025	.0014
4	.0395	.0342	.0289	.0236	.0177	.0116	.0080	.0046	.0023	.0013
5	.0282	.0252	.0222	.0192	.0142	.0095	.0065	.0039	.0021	.0012
6	.0179	.0158	.0137	.0116	.0095	.0074	.0050	.0032	.0019	.0011
7	.0125	.0110	.0095	.0080	.0065	.0050	.0035	.0025	.0017	.0010
8	.0067	.0060	.0054	.0047	.0040	.0033	.0025	.0018	.0015	.0009
9	.0029	.0027	.0025	.0023	.0021	.0019	.0017	.0015	.0013	.0008
10	.0016	.0015	.0014	.0013	.0012	.0011	.0010	.0009	.0008	.0007

TABLE I  
DEFLECTION INFLUENCE COEFFICIENT MATRICES - Continued  
(b) Model F-2

$A_{ij}$ , in./lb, at -										
$i \backslash j$	1	2	3	4	5	6	7	8	9	10
1	0.2079	0.1429	0.1011	0.0701	0.0478	0.0308	0.0175	0.0074	0.0030	0.0016
2	.1429	.1129	.0844	.0596	.0415	.0268	.0152	.0066	.0028	.0015
3	.1011	.0844	.0677	.0501	.0352	.0228	.0129	.0058	.0026	.0014
4	.0701	.0601	.0501	.0401	.0289	.0188	.0106	.0050	.0024	.0013
5	.0478	.0415	.0352	.0289	.0226	.0148	.0083	.0042	.0022	.0012
6	.0308	.0268	.0228	.0188	.0148	.0103	.0060	.0034	.0020	.0011
7	.0175	.0152	.0129	.0106	.0083	.0060	.0037	.0026	.0018	.0010
8	.0074	.0066	.0058	.0050	.0042	.0034	.0026	.0018	.0015	.0009
9	.0030	.0028	.0026	.0024	.0022	.0020	.0018	.0016	.0014	.0008
10	.0016	.0015	.0014	.0013	.0012	.0011	.0010	.0009	.0008	.0007

TABLE I  
DEFLECTION INFLUENCE COEFFICIENT MATRICES - Concluded  
(c) Model BF

$A_{ij}$ , in./lb, at -										
$j \backslash i$	1	2	3	4	5	6	7	8	9	10
1	0.1272	0.0884	0.0637	0.0458	0.0322	0.0209	0.0118	0.0054	0.0029	0.0016
2	.0884	.0694	.0533	.0392	.0277	.0180	.0104	.0048	.0027	.0015
3	.0637	.0533	.0429	.0326	.0232	.0151	.0090	.0042	.0025	.0014
4	.0458	.0392	.0326	.0260	.0187	.0122	.0076	.0036	.0023	.0013
5	.0322	.0277	.0232	.0187	.0142	.0093	.0062	.0030	.0021	.0012
6	.0209	.0180	.0151	.0122	.0093	.0064	.0048	.0024	.0019	.0011
7	.0118	.0104	.0090	.0076	.0062	.0048	.0034	.0018	.0017	.0010
8	.0054	.0048	.0042	.0036	.0030	.0024	.0018	.0012	.0015	.0009
9	.0029	.0027	.0025	.0023	.0021	.0019	.0017	.0015	.0015	.0008
10	.0016	.0015	.0014	.0013	.0012	.0011	.0010	.0009	.0005	.0007

CONFIDENTIAL

Models	Wing area, sq in.	Aspect ratio	$\bar{c}$ , in.
AR, AF-1, AF-2	30.54	0.848	8.00
BR, BF	15.27	0.424	8.00
CR	15.27	0.848	5.658

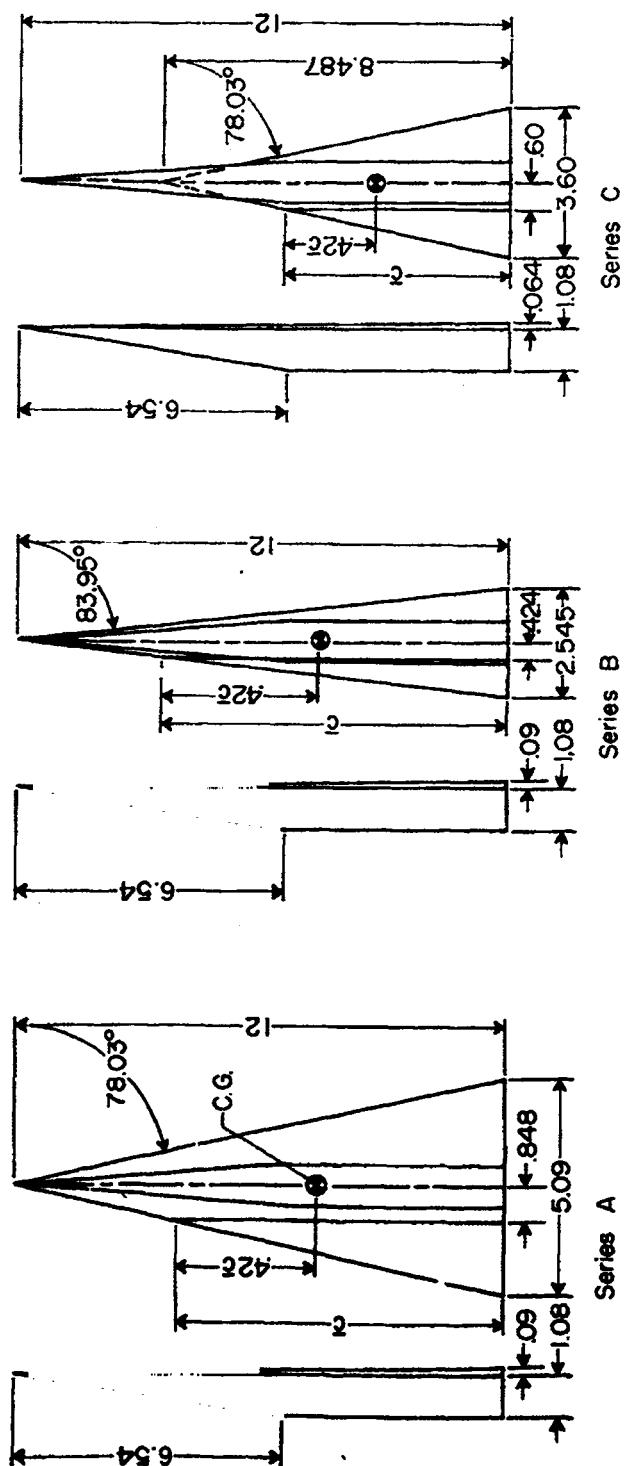
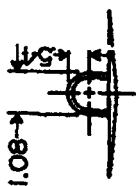


Figure 1.- Line drawings of models. All dimensions in inches.

L-694

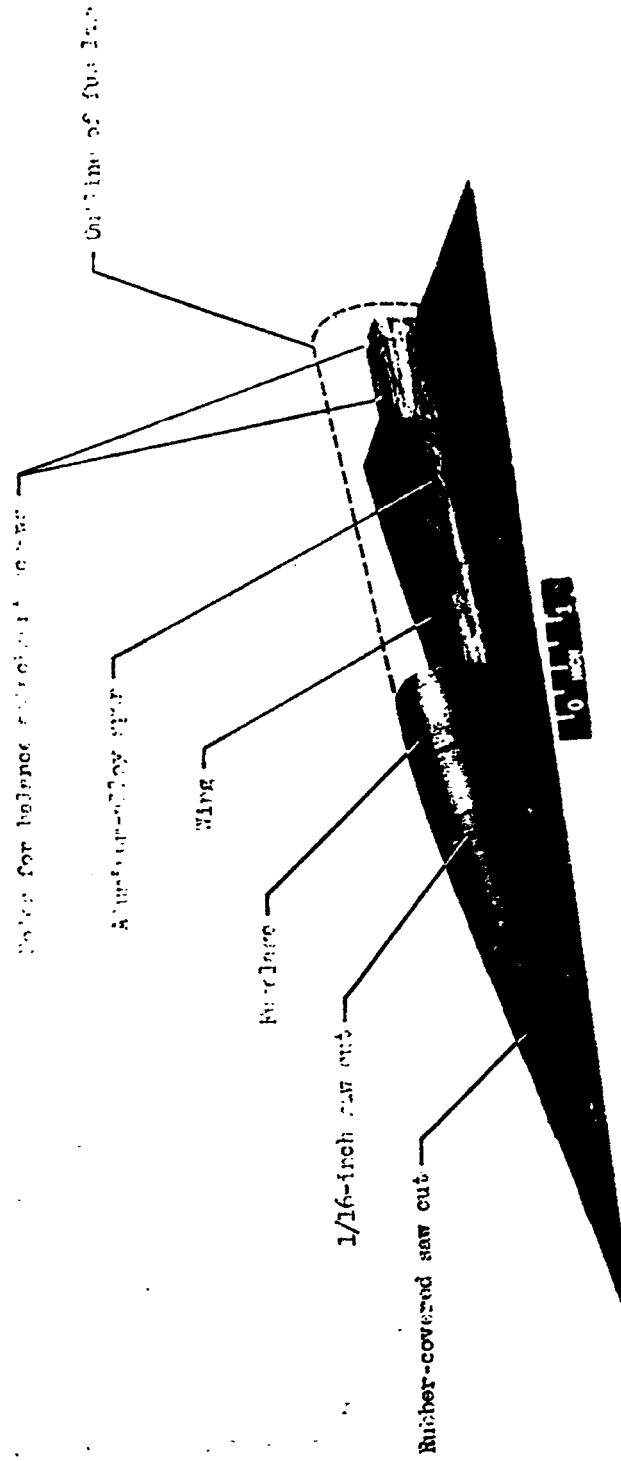


Figure 2.- Photograph of a typical flexible model of series A with part of fuselage removed to show details of model construction.

L-59-2994.1



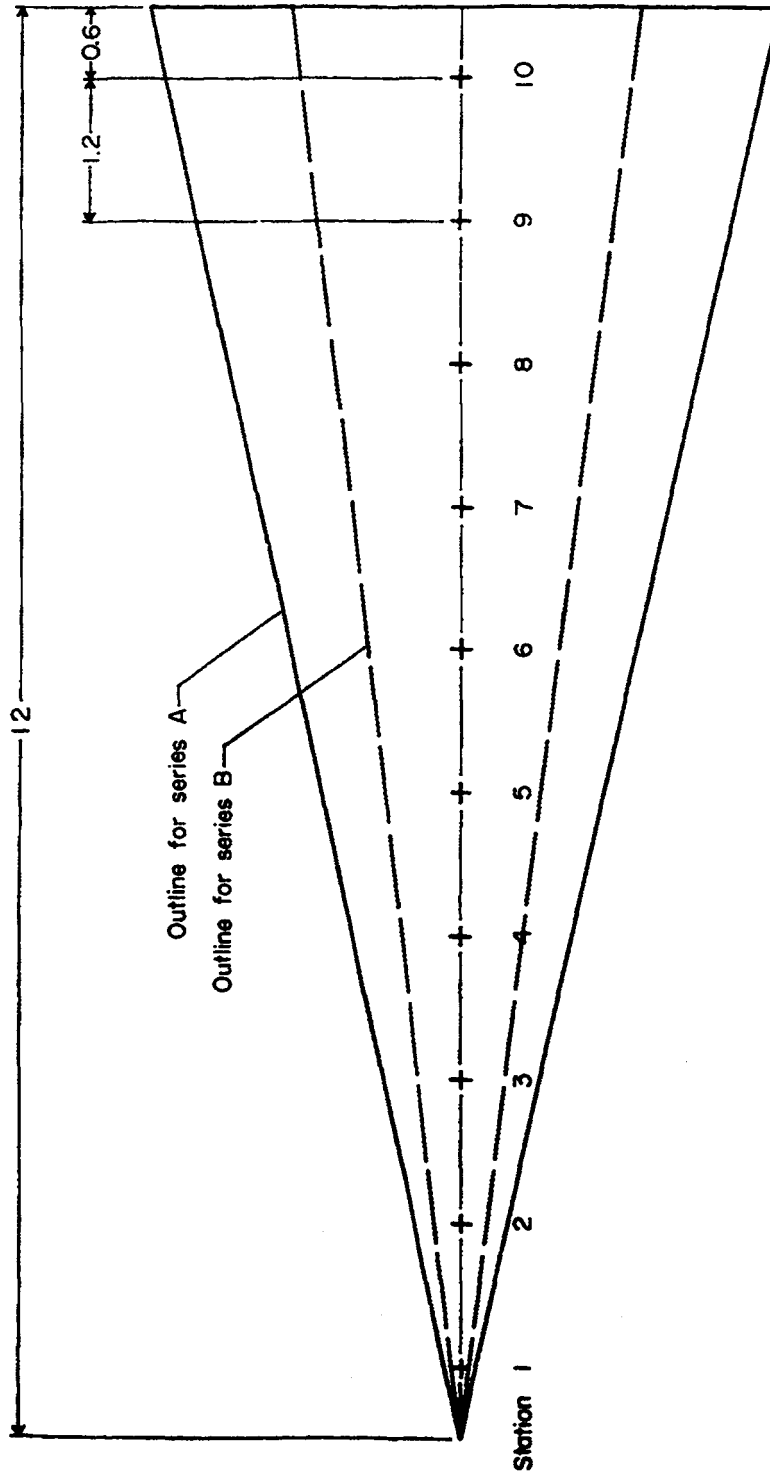


Figure 3.- Location of points on model at which influence coefficients were measured. All dimensions in inches.

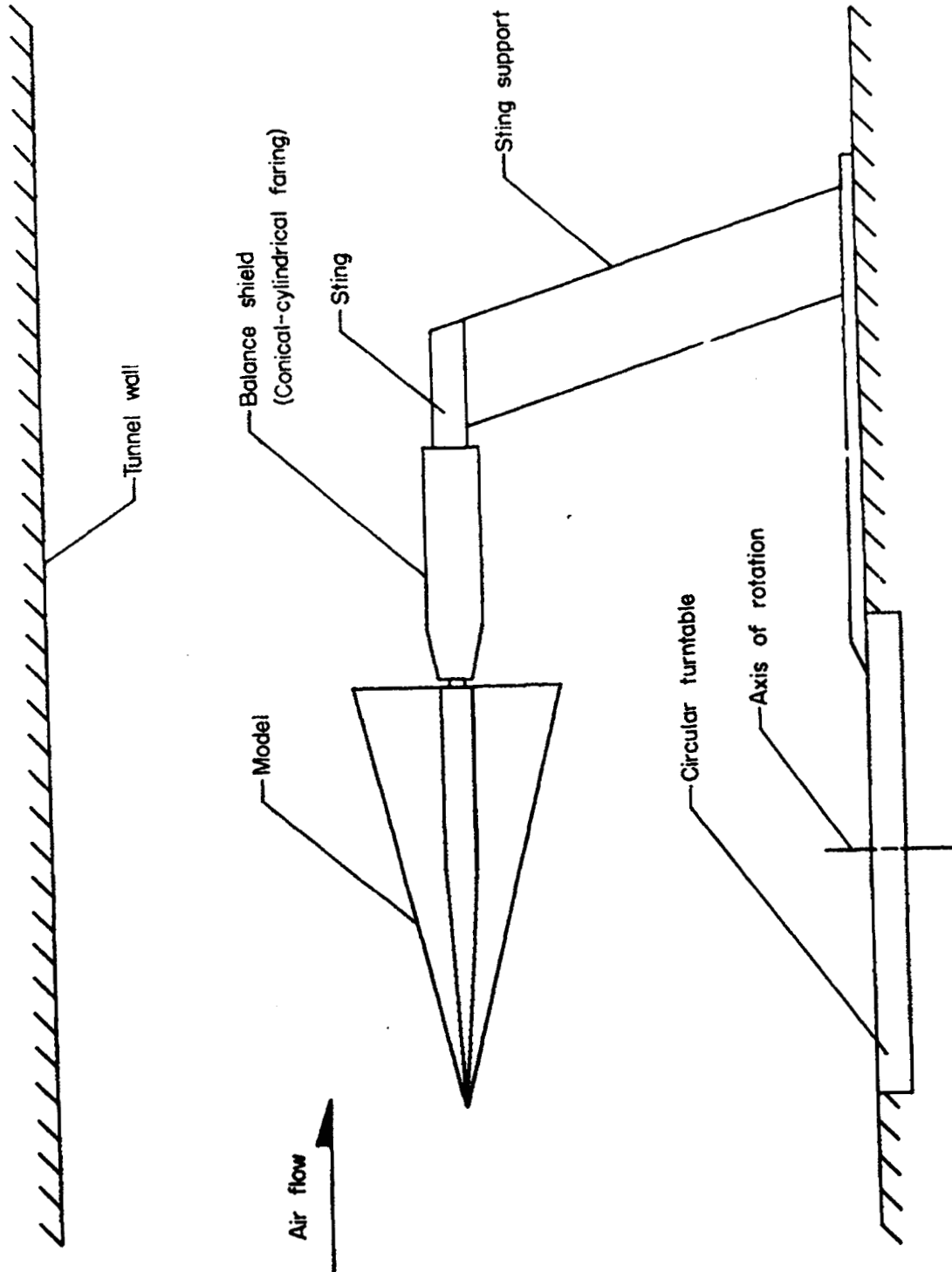


Figure 4.- Planform of model support system.

037124030

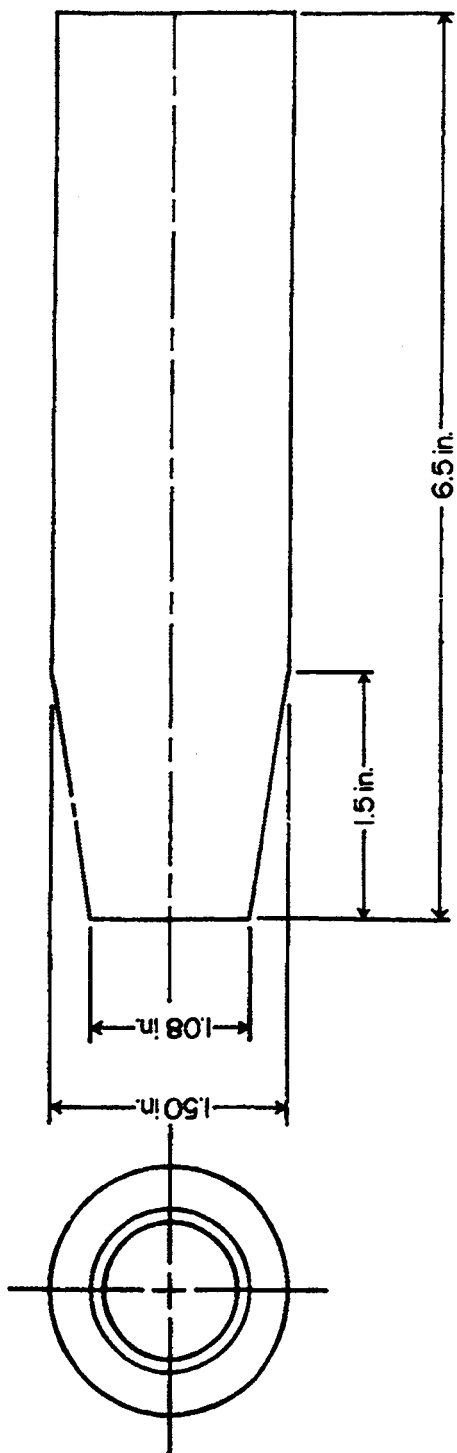


Figure 5.- Line drawing of balance shield.

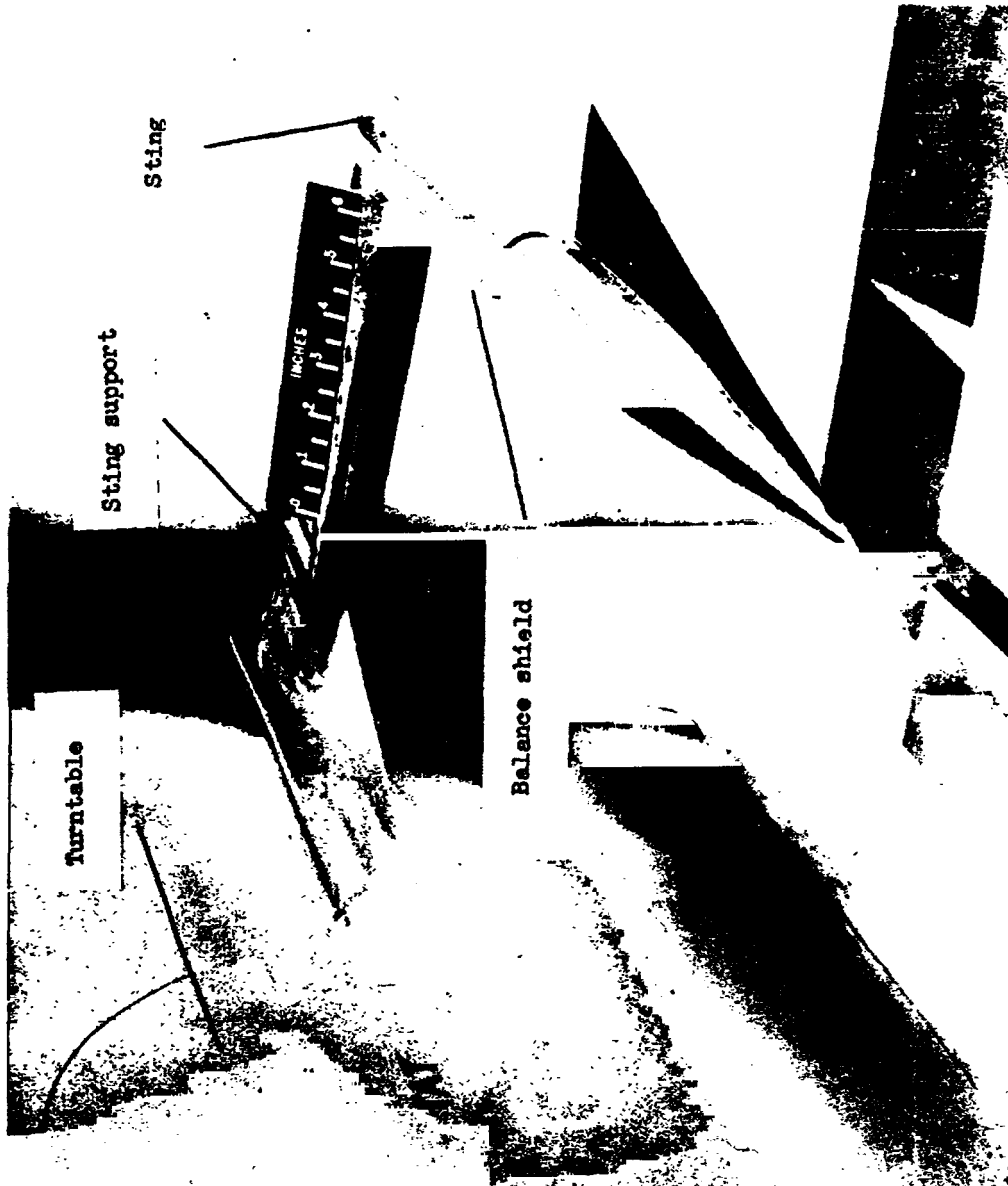


Figure 6.- Photograph of typical model mounted in test section. L-59-2634.1

CONFIDENTIAL

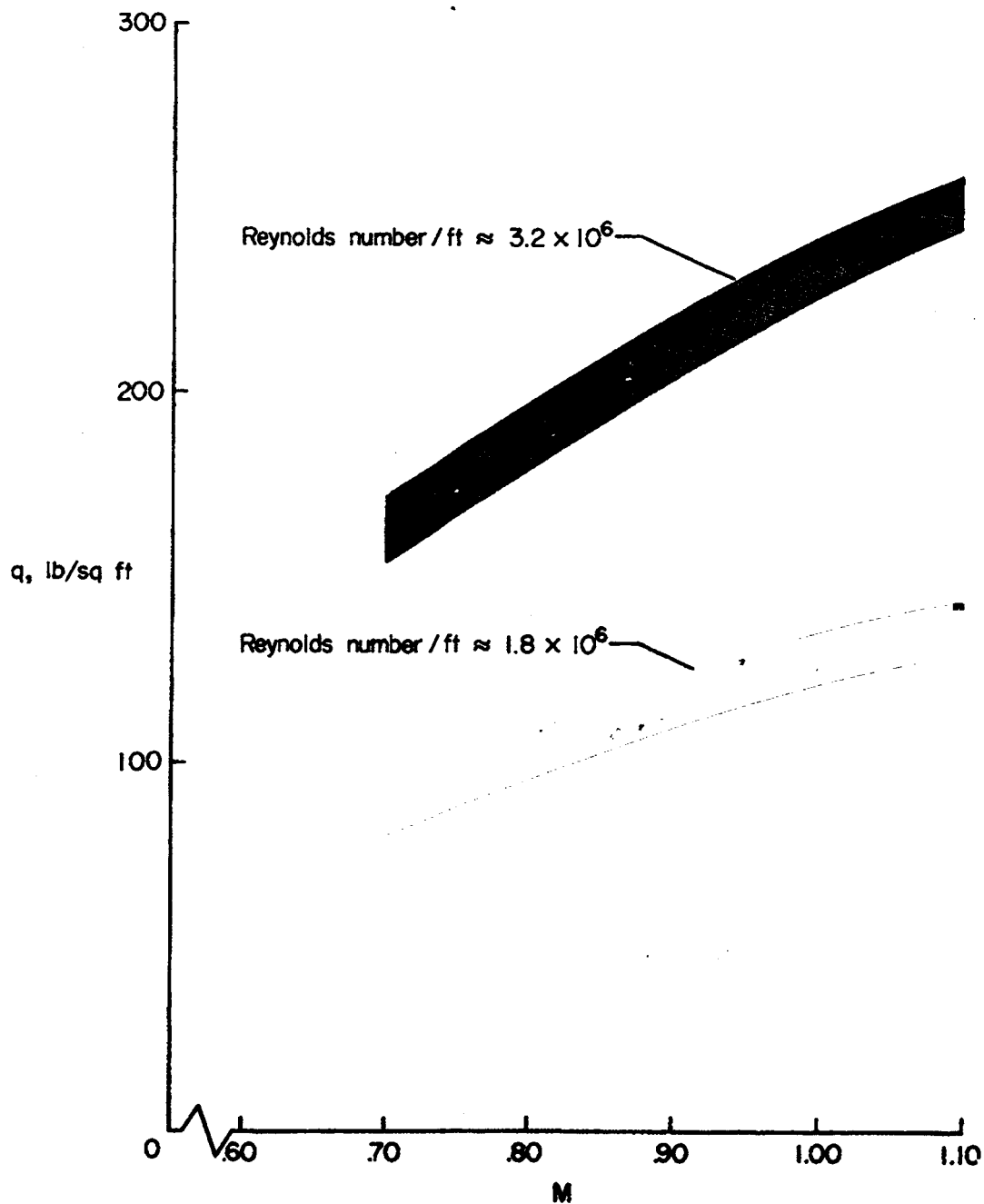
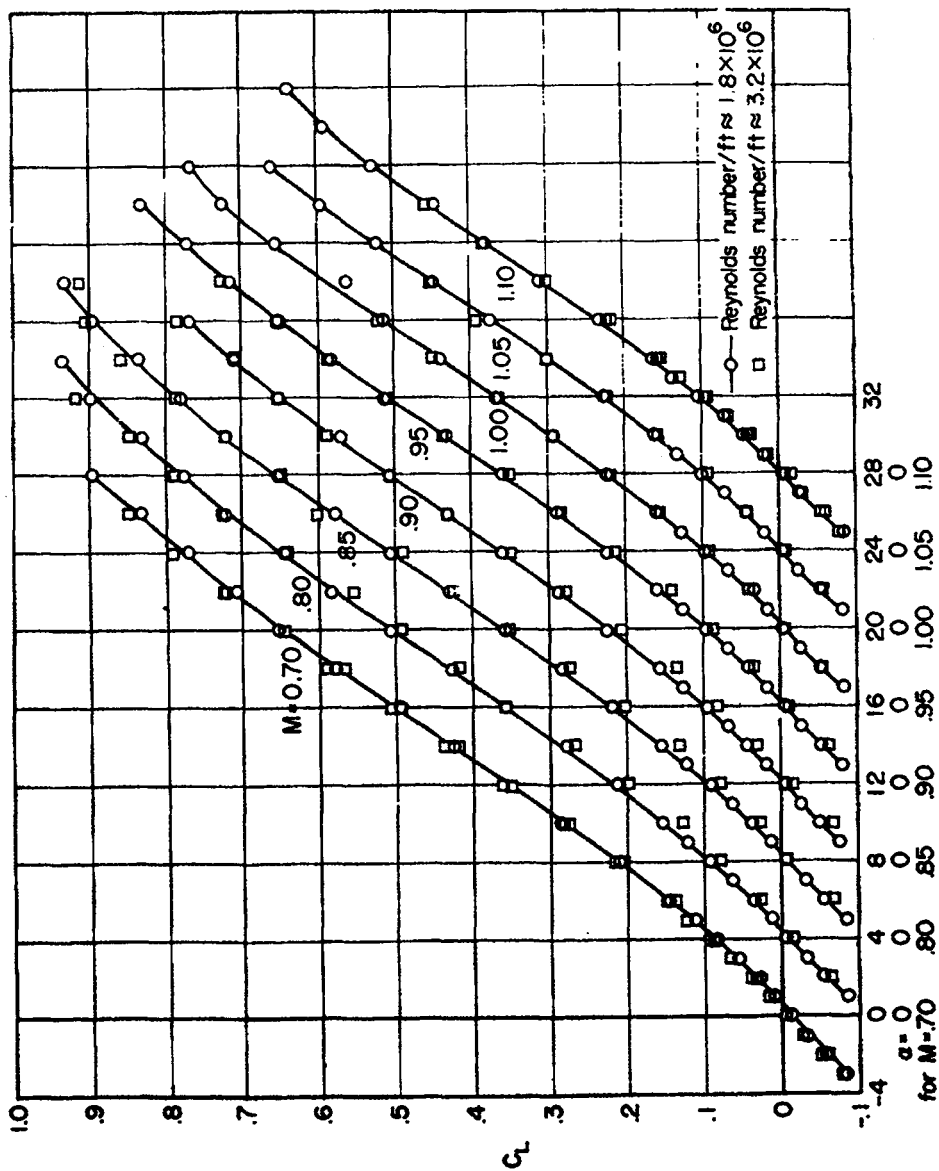
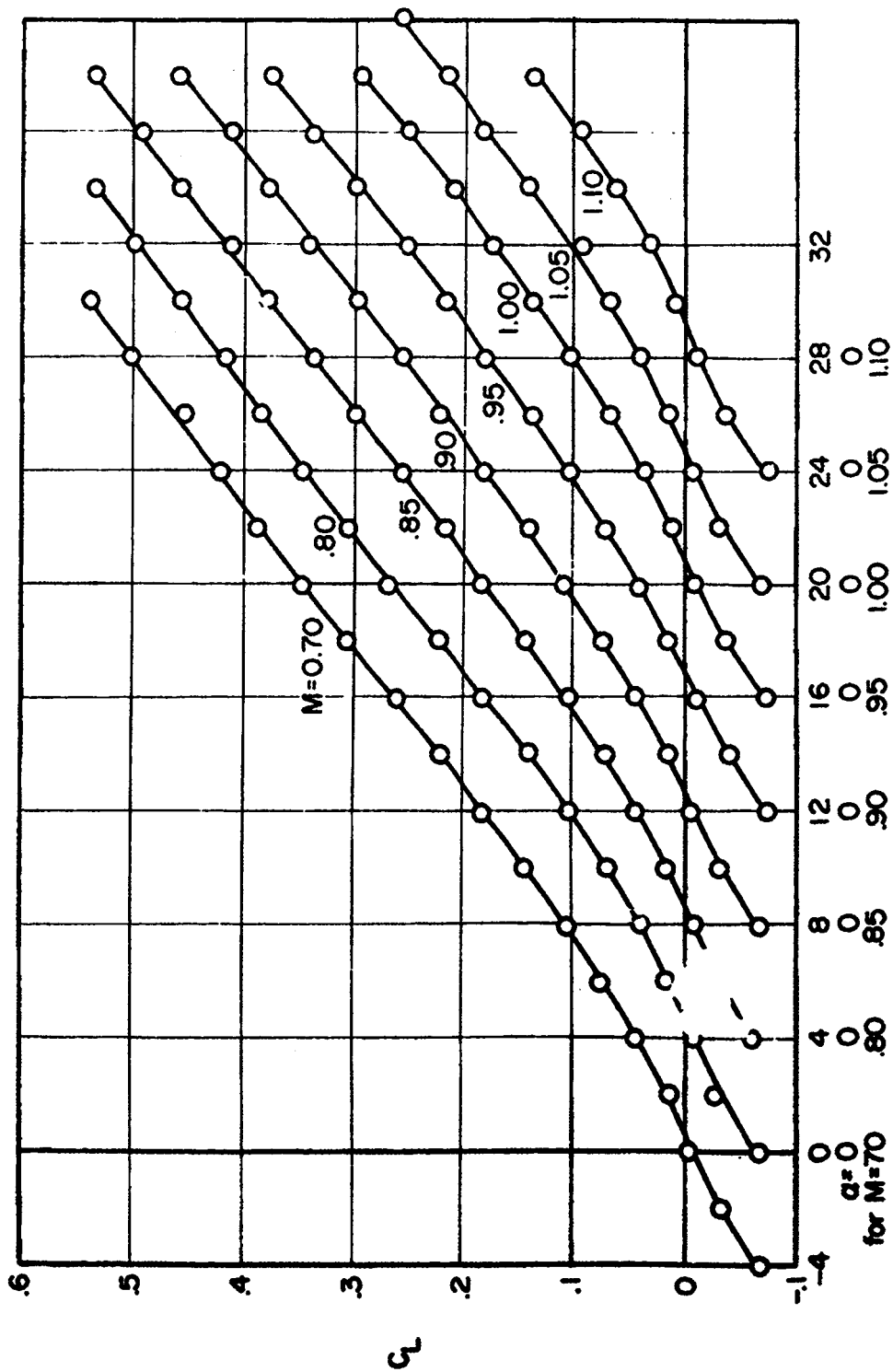


Figure 7.- Variation of dynamic pressure with Mach number for both test Reynolds numbers.



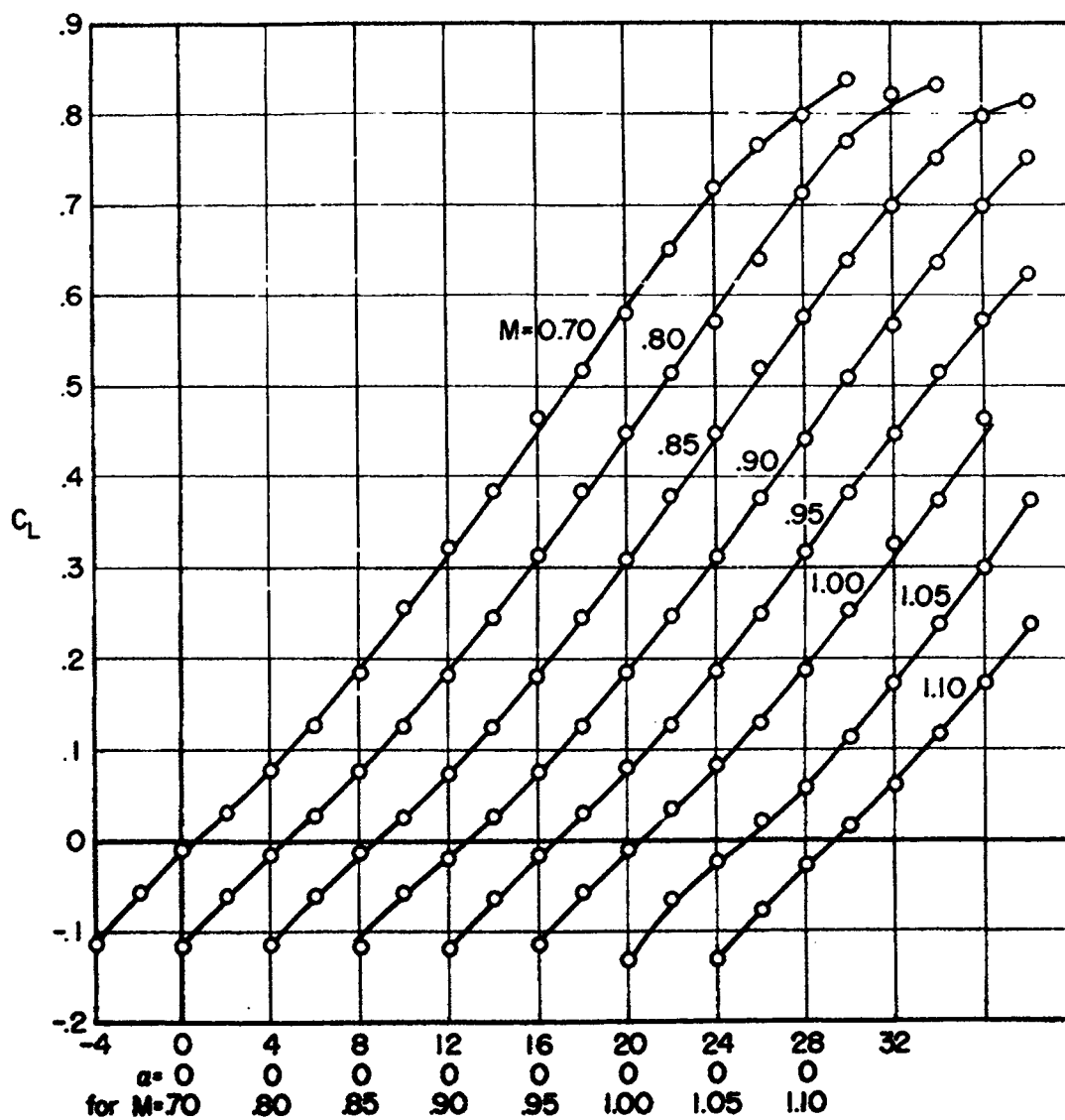
(a) Model AR.

Figure 8.- Variation of lift coefficient with angle of attack for rigid models.



(b) Model BR. Reynolds number per foot  $\approx 3.2 \times 10^6$ .

Figure 8.- Continued.



(c) Model CR. Reynolds number per foot  $\approx 3.2 \times 10^6$ .

Figure 8.- Concluded.



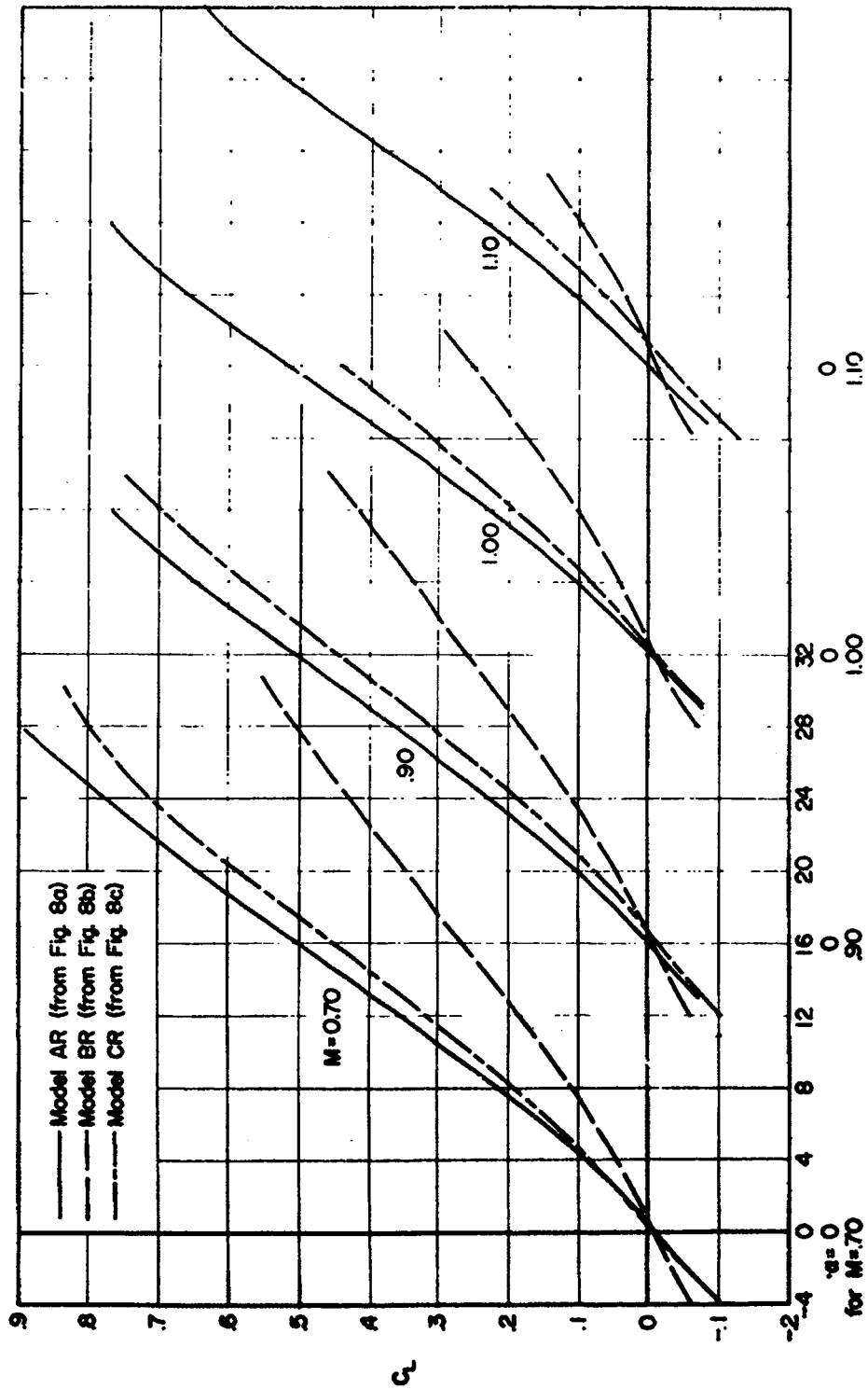
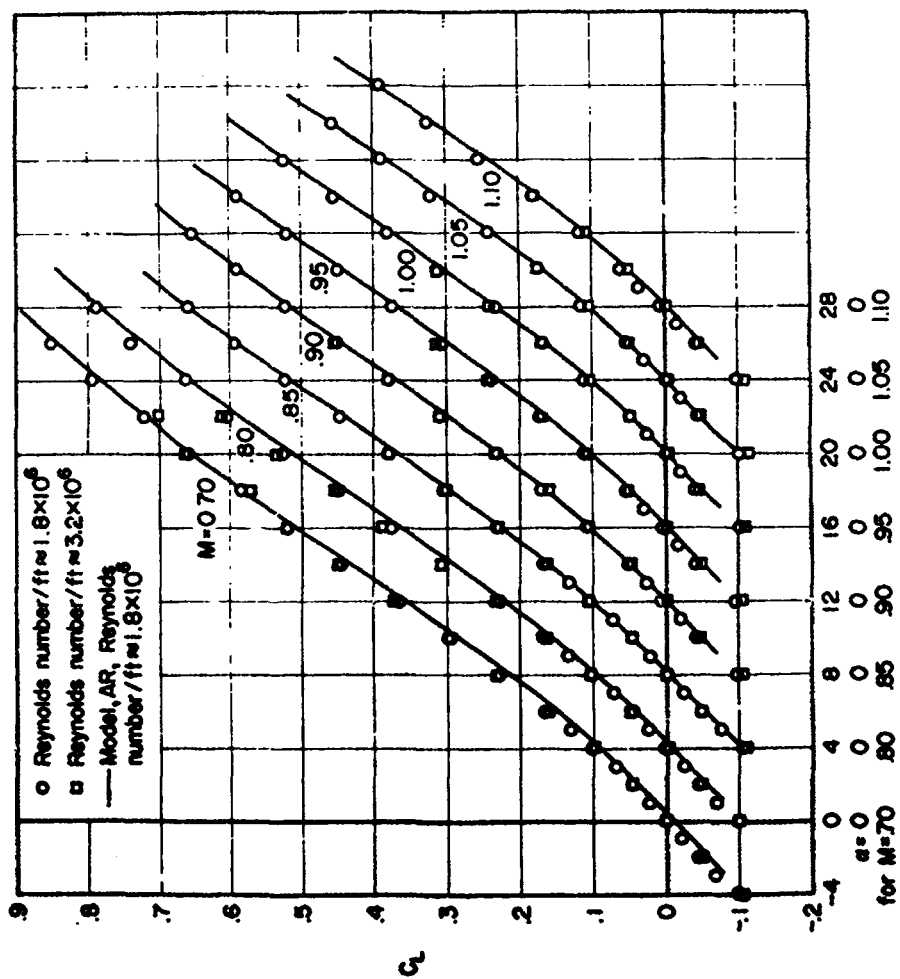
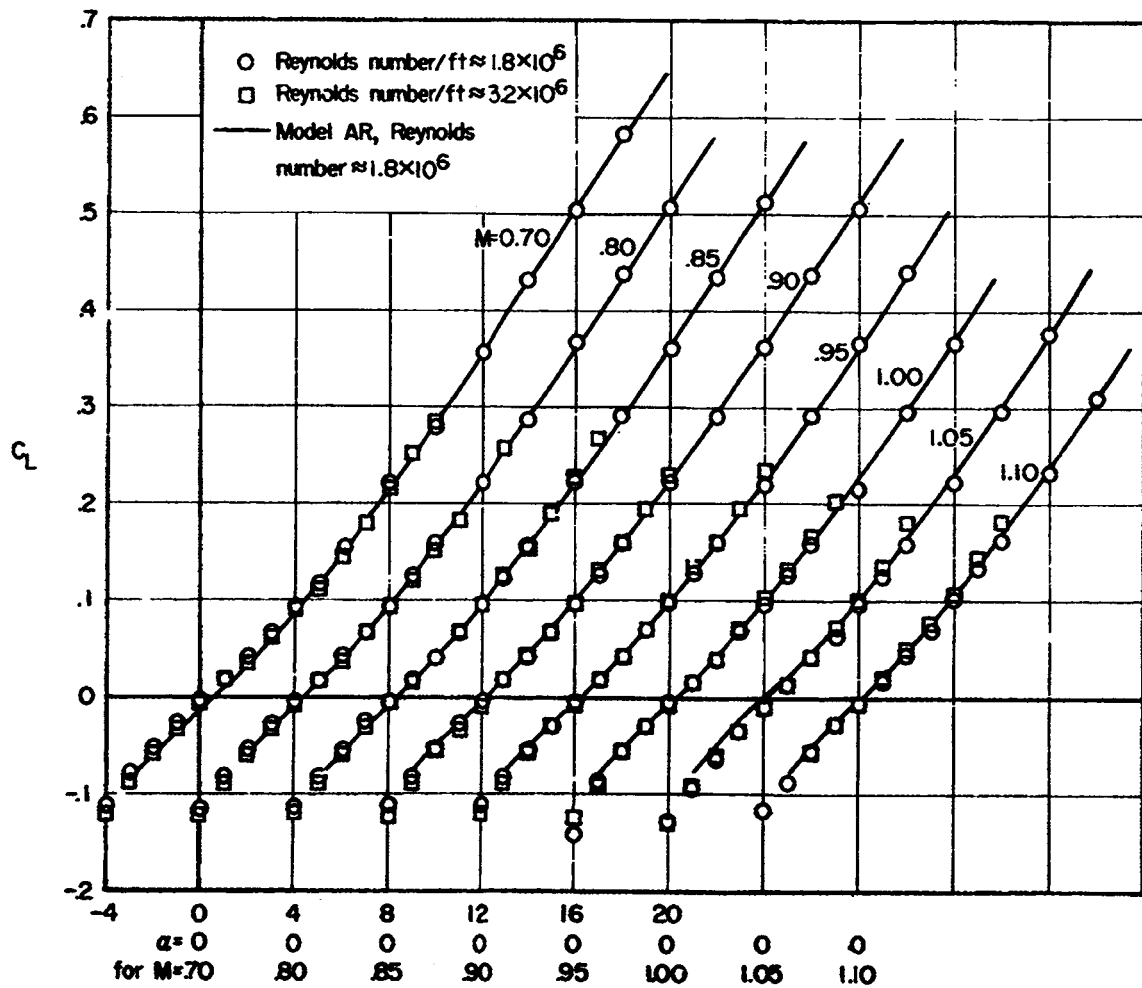


Figure 9.- Comparison of the variation of lift coefficient with angle of attack at several Mach numbers for models AR, BR, and CR.



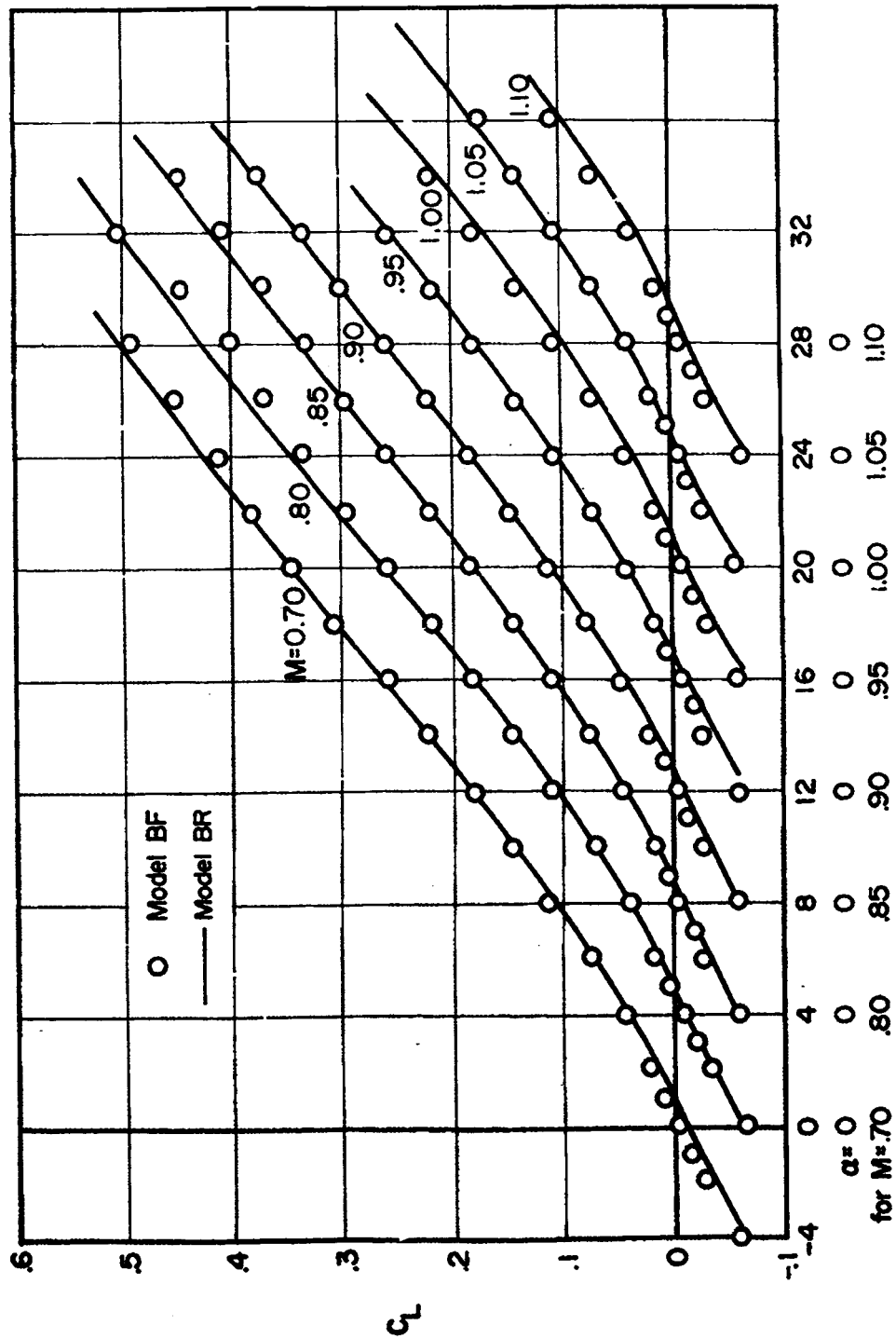
(a) Model AF-1.

Figure 10.- Variation of lift coefficient with angle of attack for flexible models of series A and series B, and a comparison with rigid-model curves from figure 8.



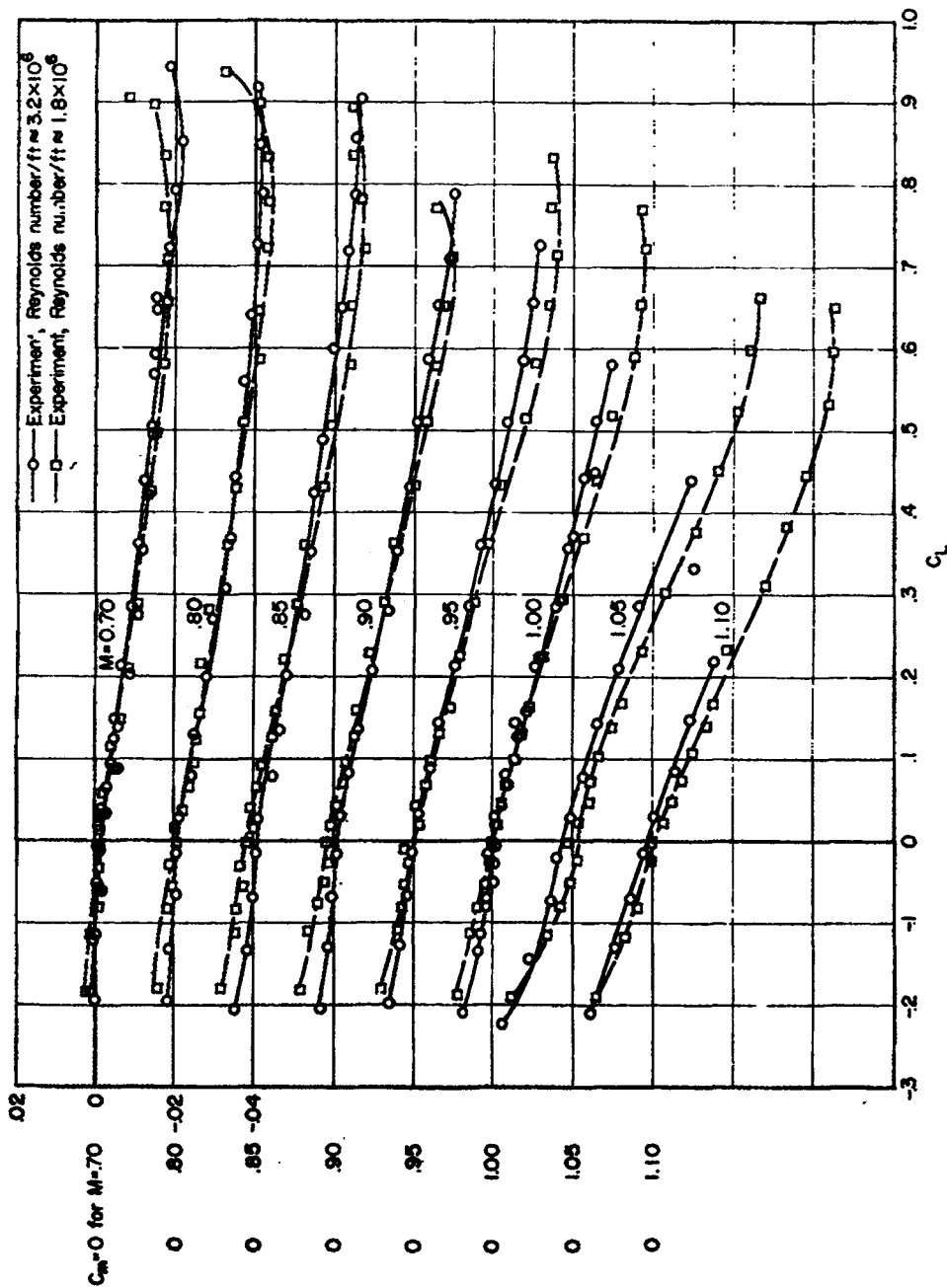
(b) Model AF-2.

Figure 10.- Continued.



(c) Model BF.

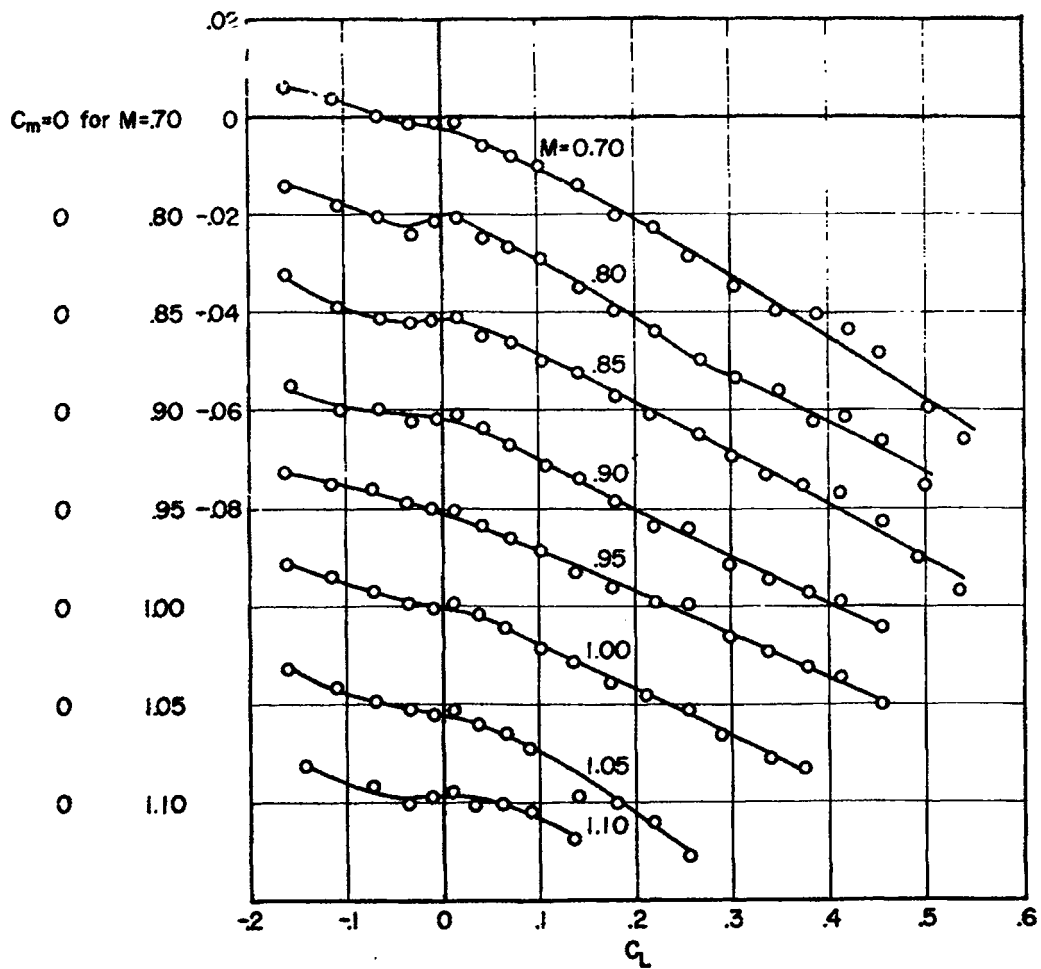
Figure 10.- Concluded.



(a) Model AR.

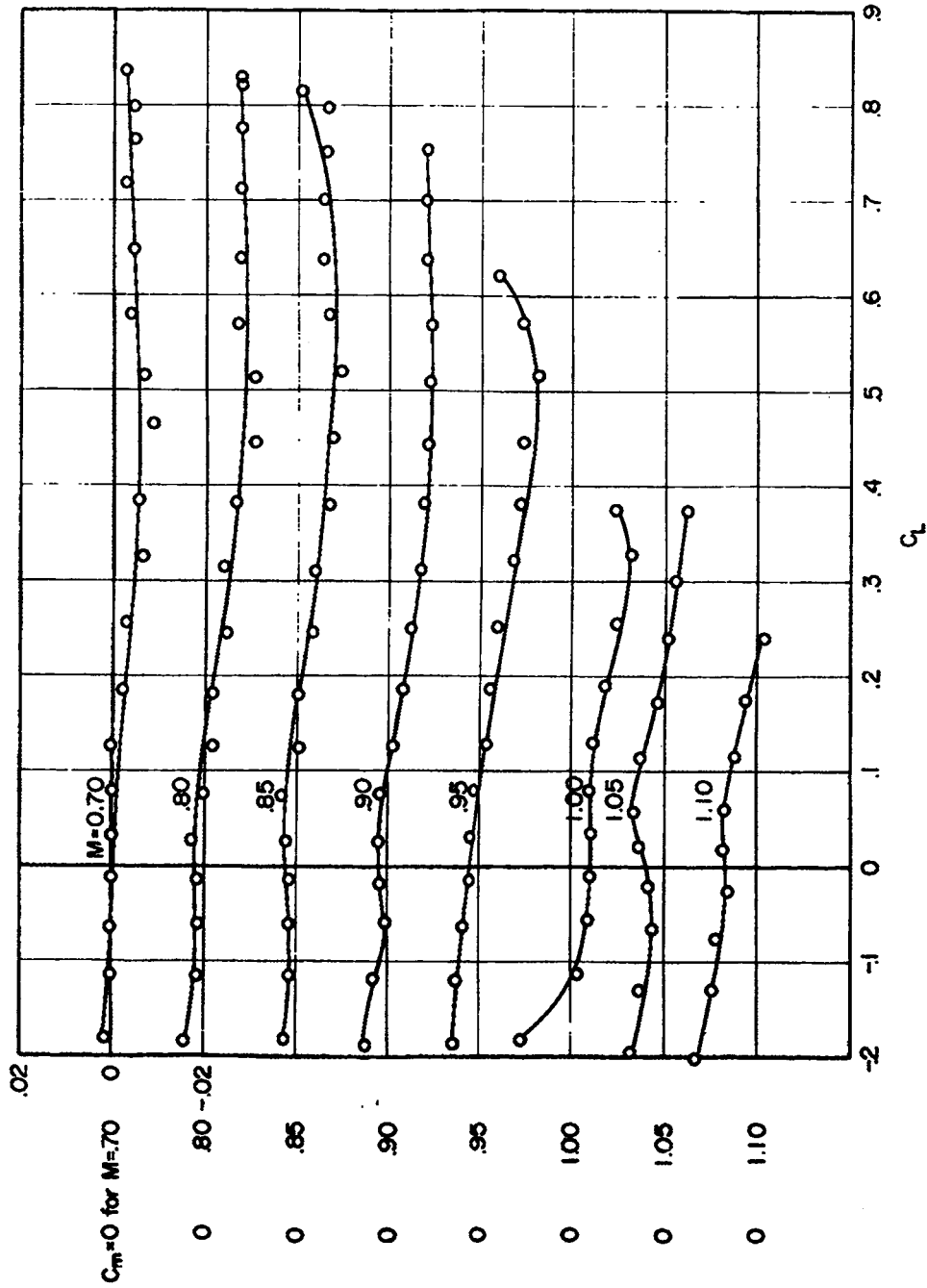
Figure 11.- Variation of pitching-moment coefficient with lift coefficient for rigid models.

CONFIDENTIAL



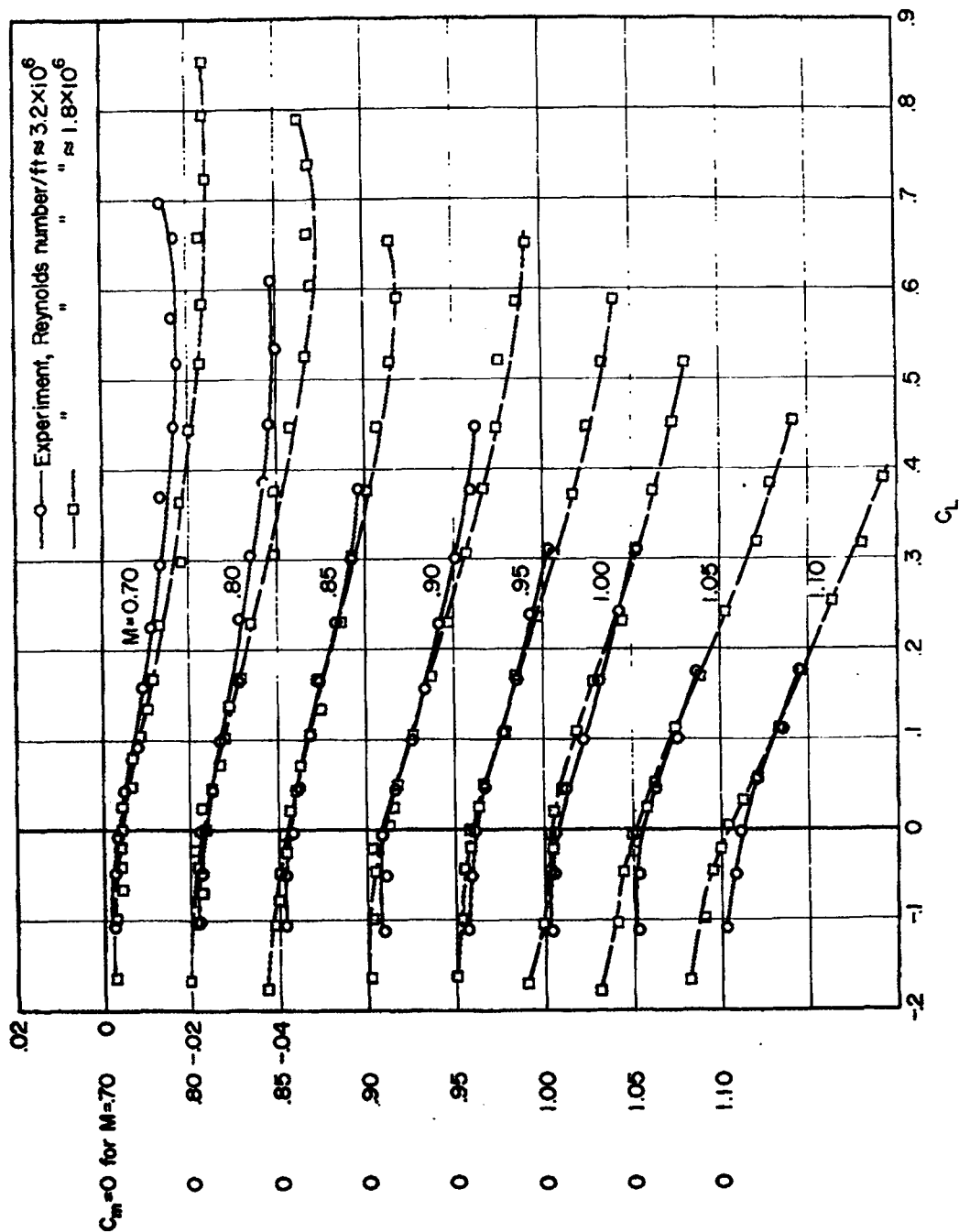
(b) Model BR. Reynolds number per foot  $\approx 3.2 \times 10^6$ .

Figure 11.- Continued.



(c) Model CR. Reynolds number per foot  $\approx 3.2 \times 10^6$ .

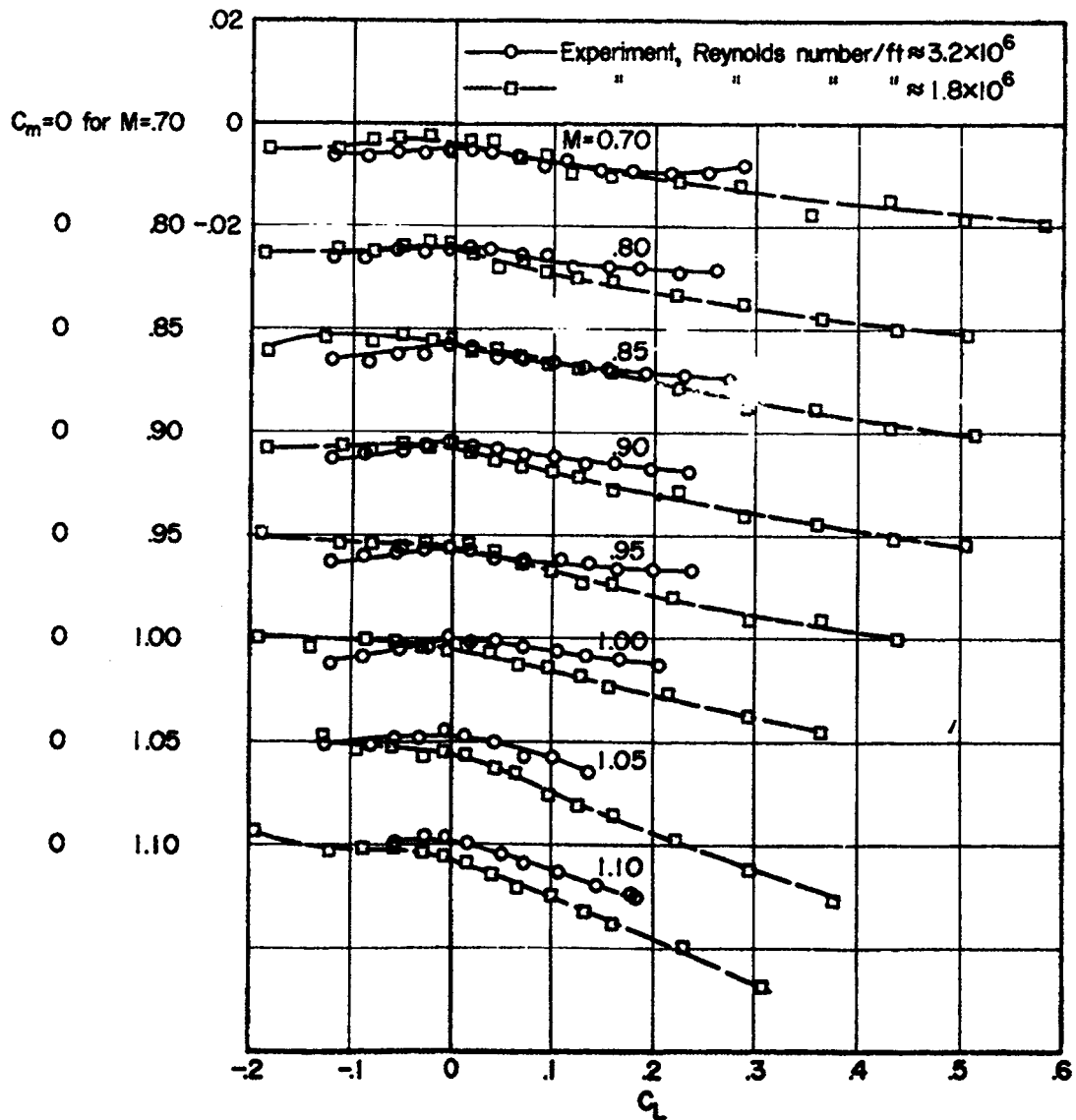
Figure 11.- Concluded.



(a) Model AF-1.

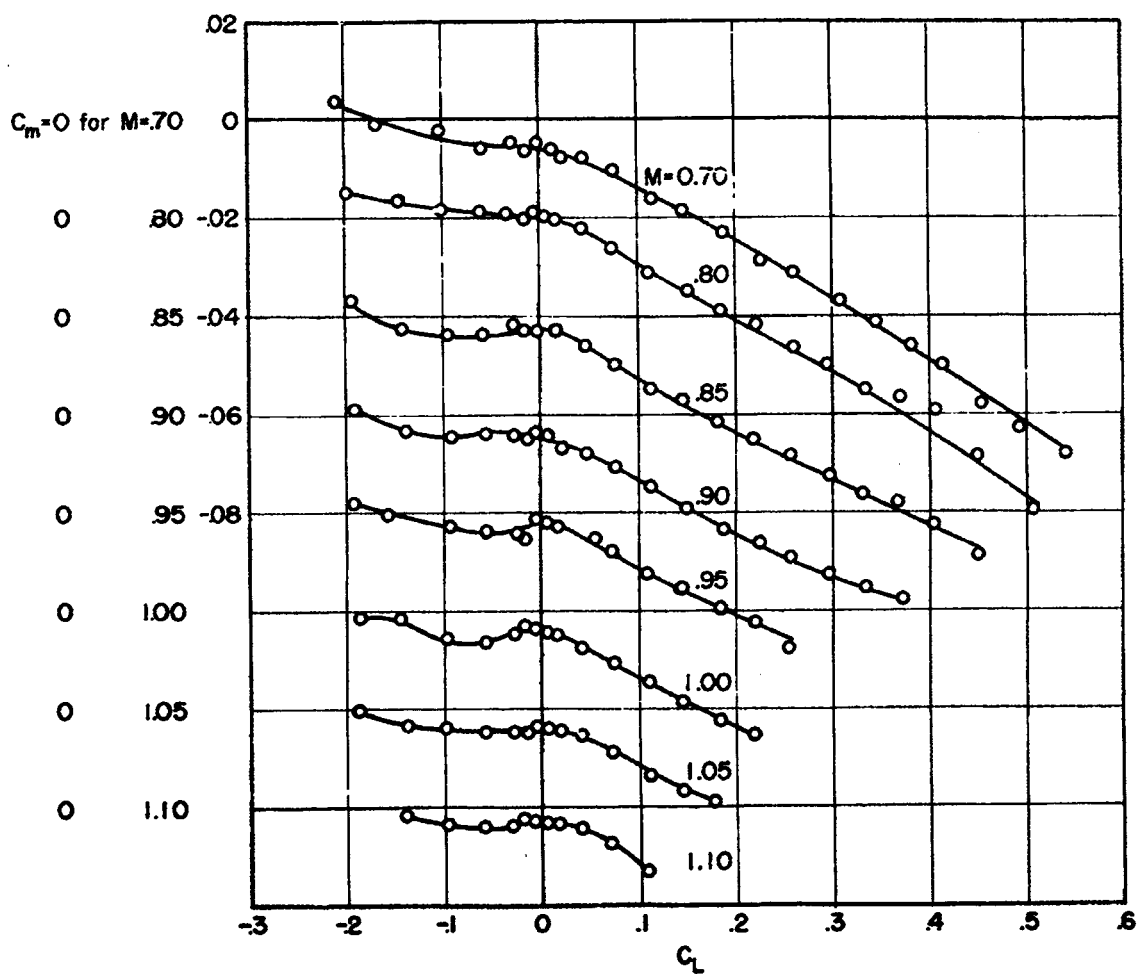
Figure 12.- Variation of pitching-moment coefficient with lift coefficient for flexible models.





(b) Model AF-2.

Figure 12.- Continued.



(c) Model BF. Reynolds number per foot  $\approx 3.2 \times 10^6$ .

Figure 12.- Concluded.

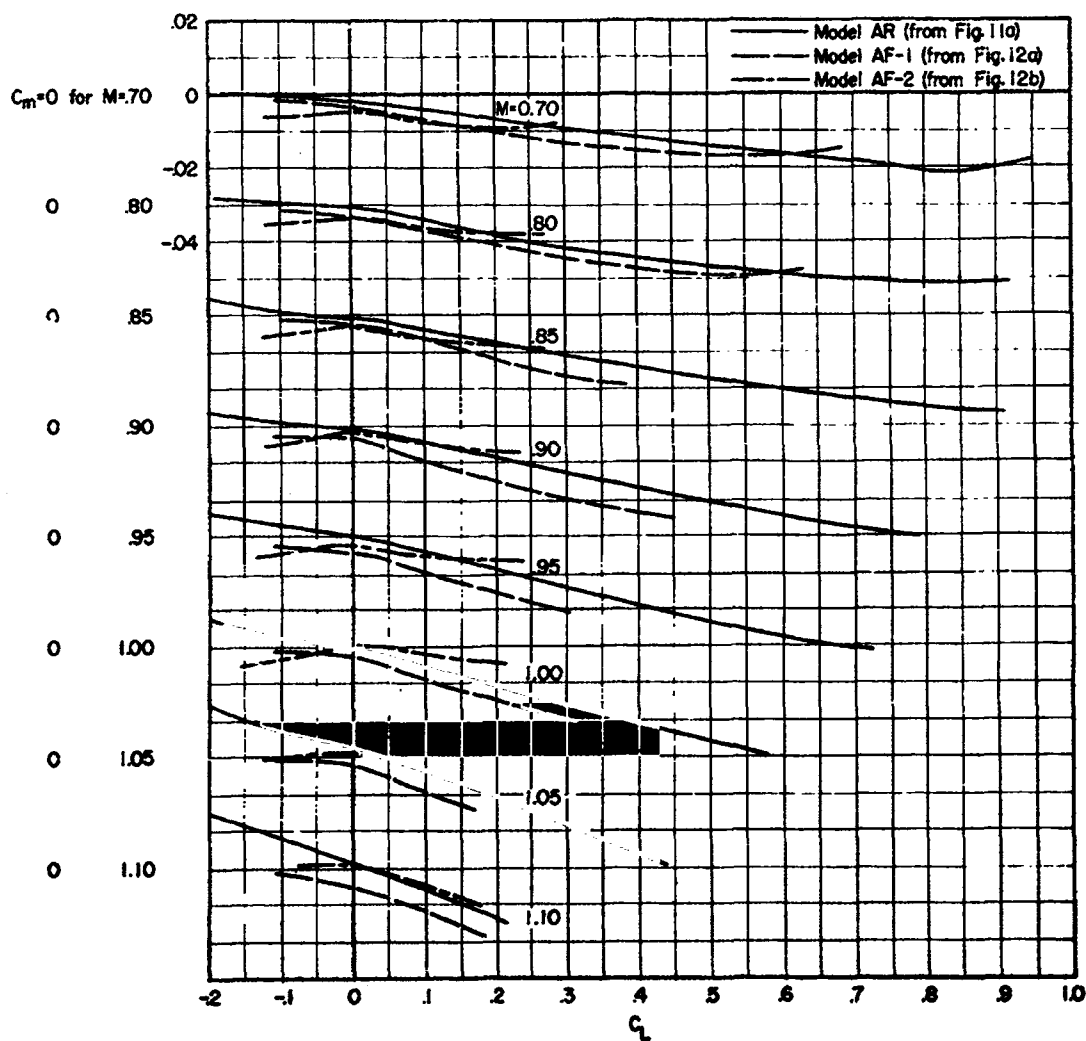
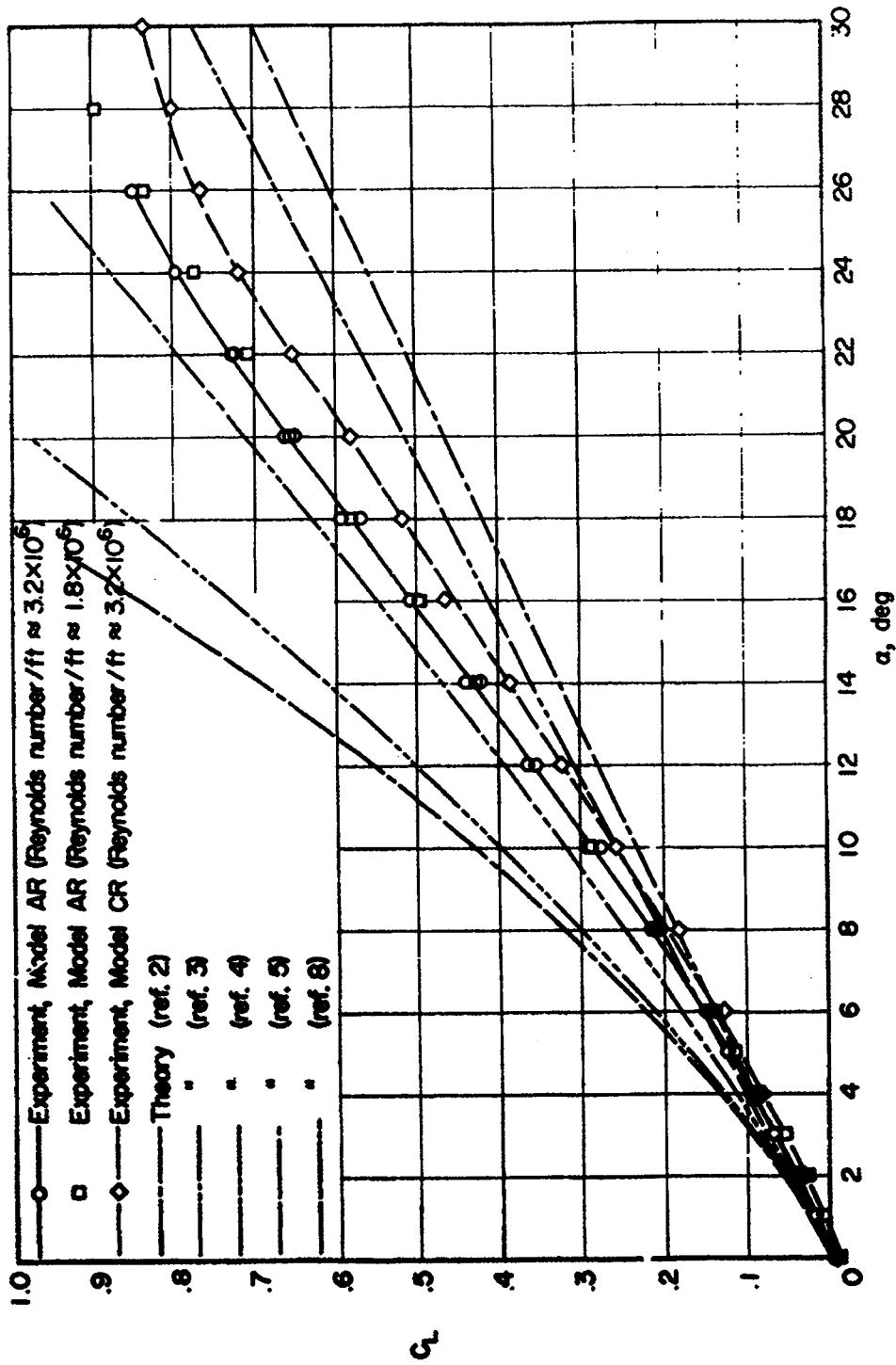


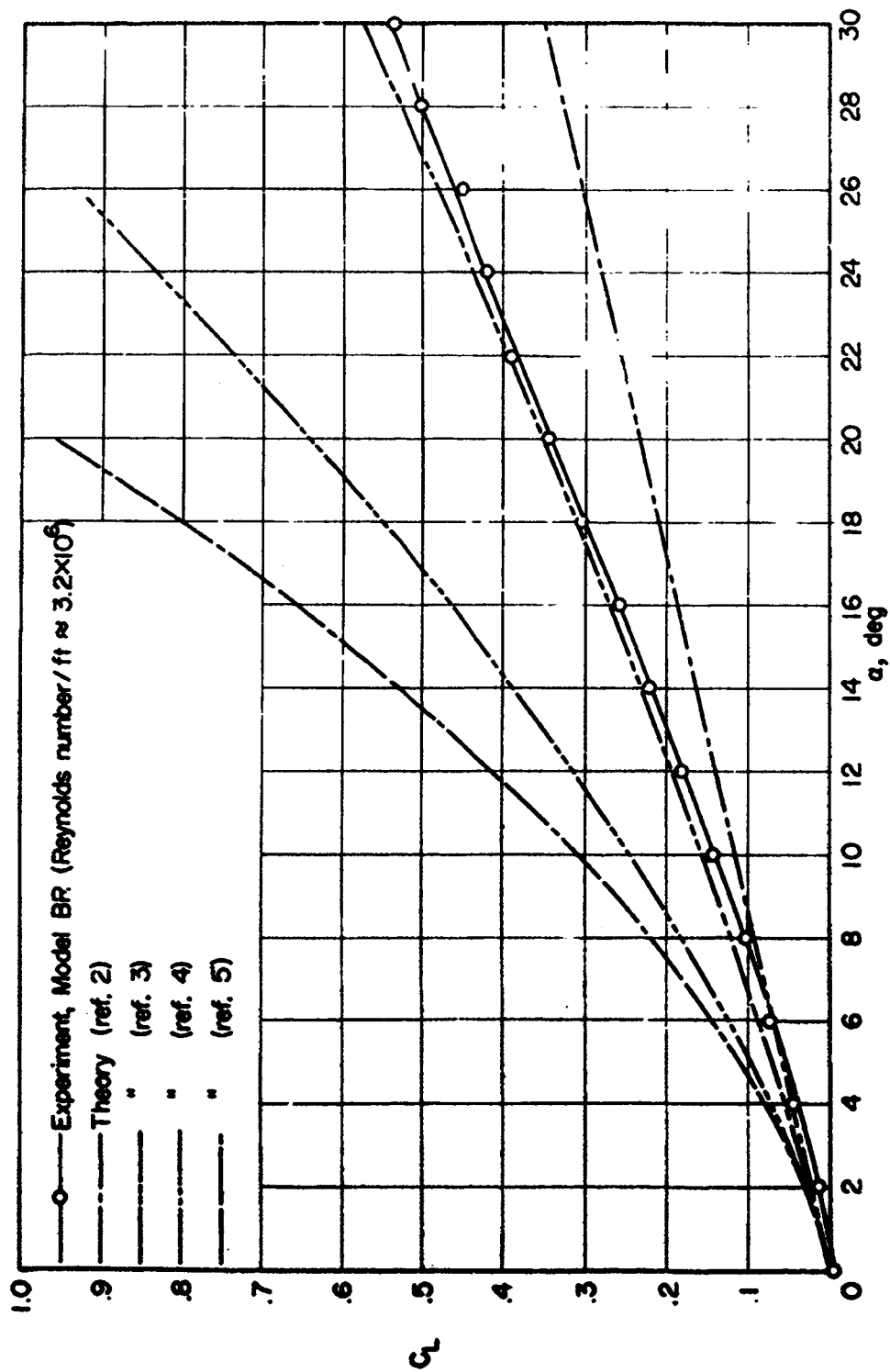
Figure 13.- Comparison of variation of pitching-moment coefficient with lift coefficient for models of series A.

Reynolds number per foot  $\approx 3.2 \times 10^6$ .



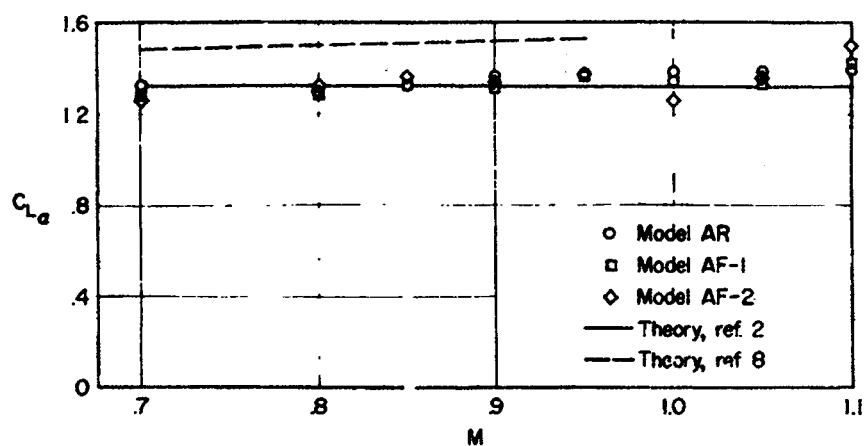
(a) Models AR and CR.

Figure 14.- Comparison of measured and calculated lift coefficients.  $M = 0.70$ .

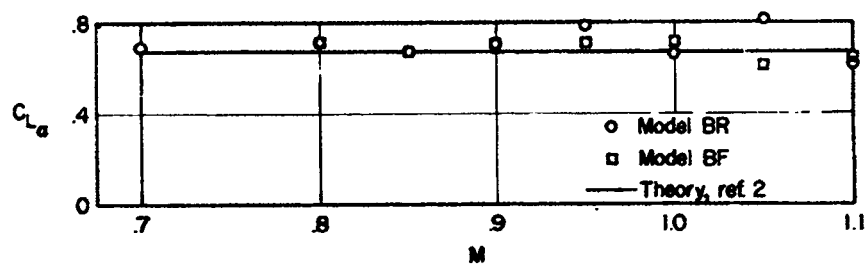


(b) Model BR.

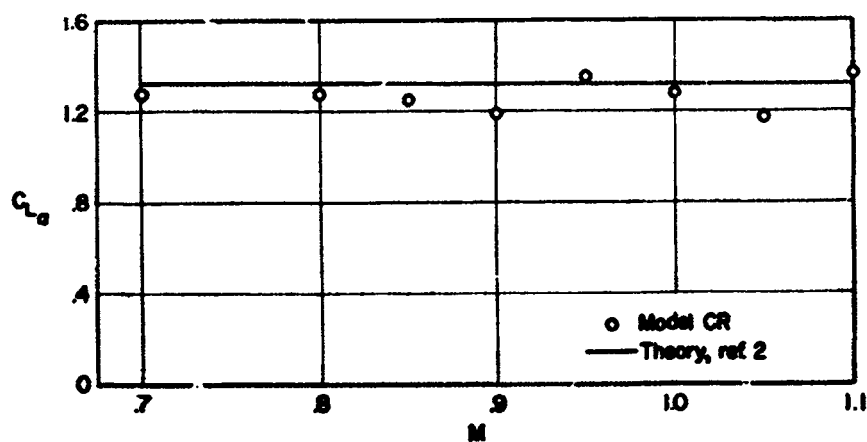
Figure 14.- Concluded.



(a) Series A.



(b) Series B.



(c) Series C.

Figure 15.- Variation of lift-curve slope at zero-lift condition with Mach number. Reynolds number per foot  $\approx 3.2 \times 10^6$ .

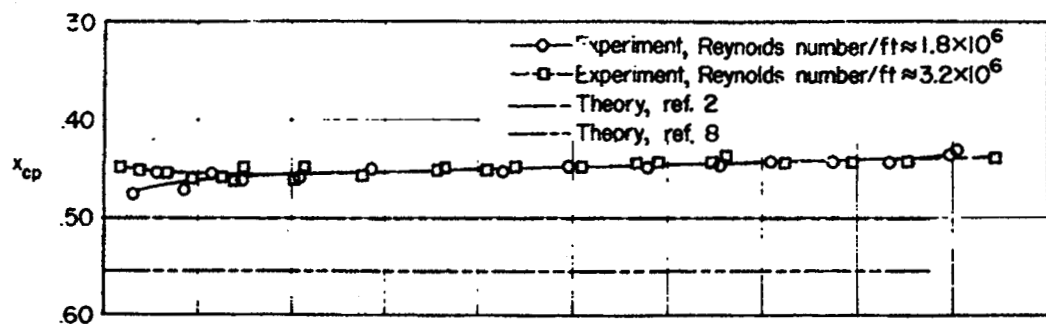
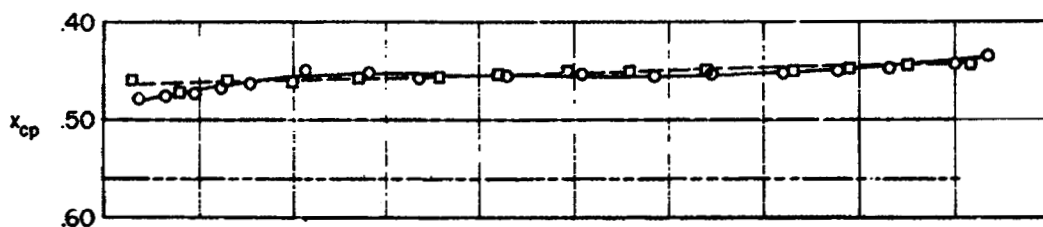
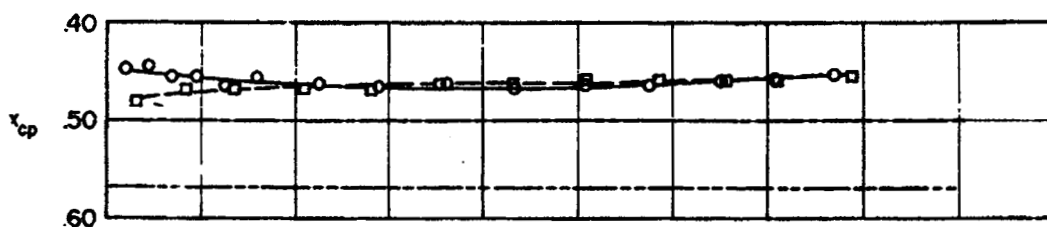
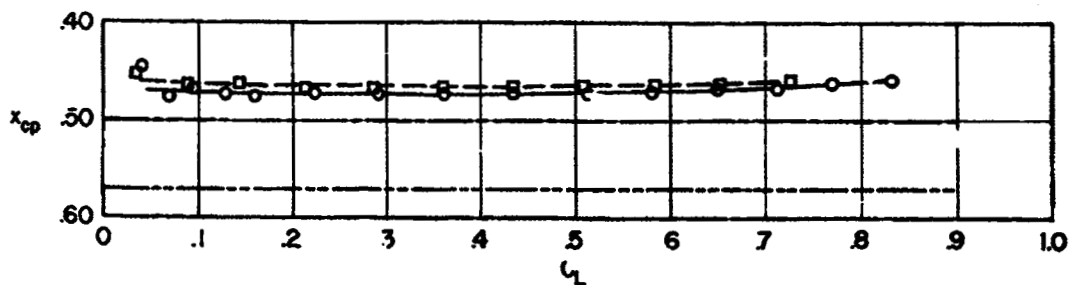
(a)  $M = 0.70$ .(b)  $M = 0.80$ .(c)  $M = 0.90$ .(d)  $M = 0.95$ .

Figure 16.- Variation of center-of-pressure location for model A2 with lift coefficient at several  $M_\infty$  numbers.

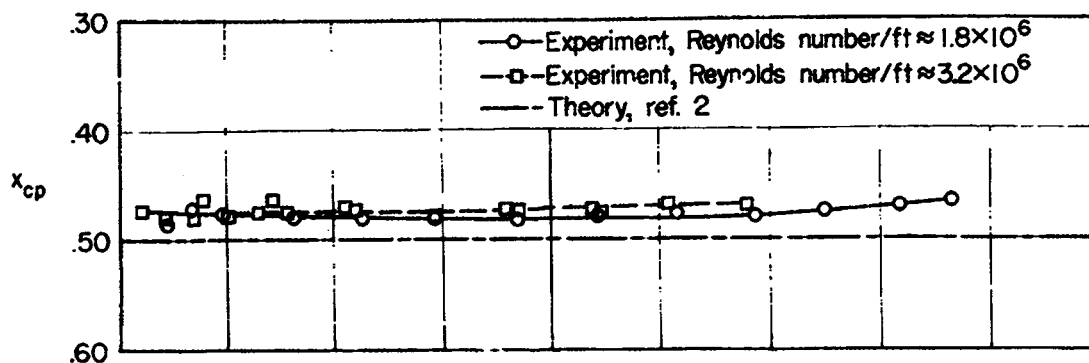
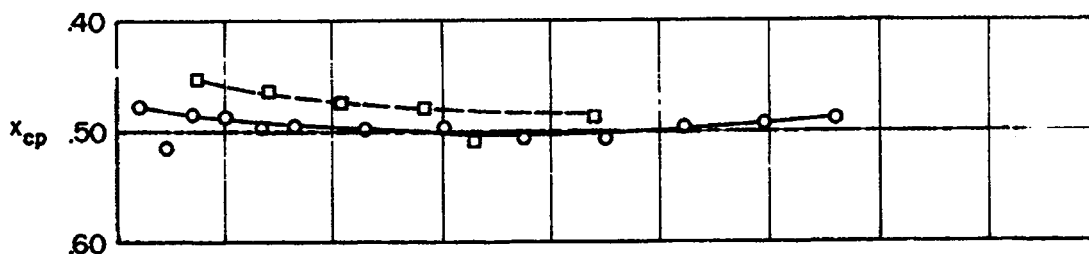
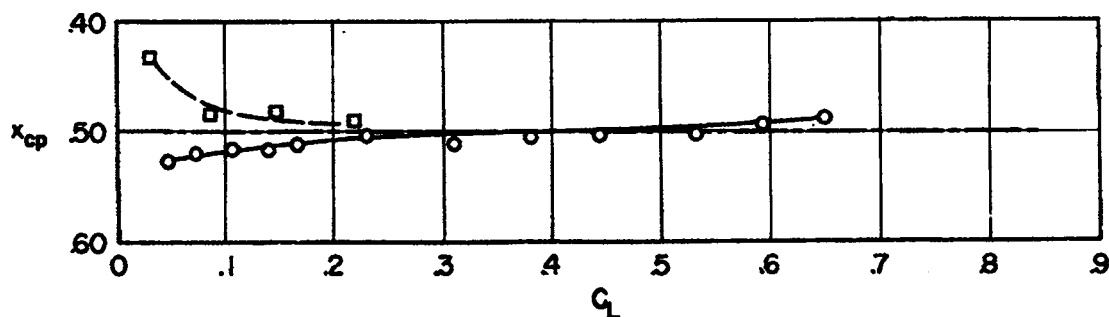
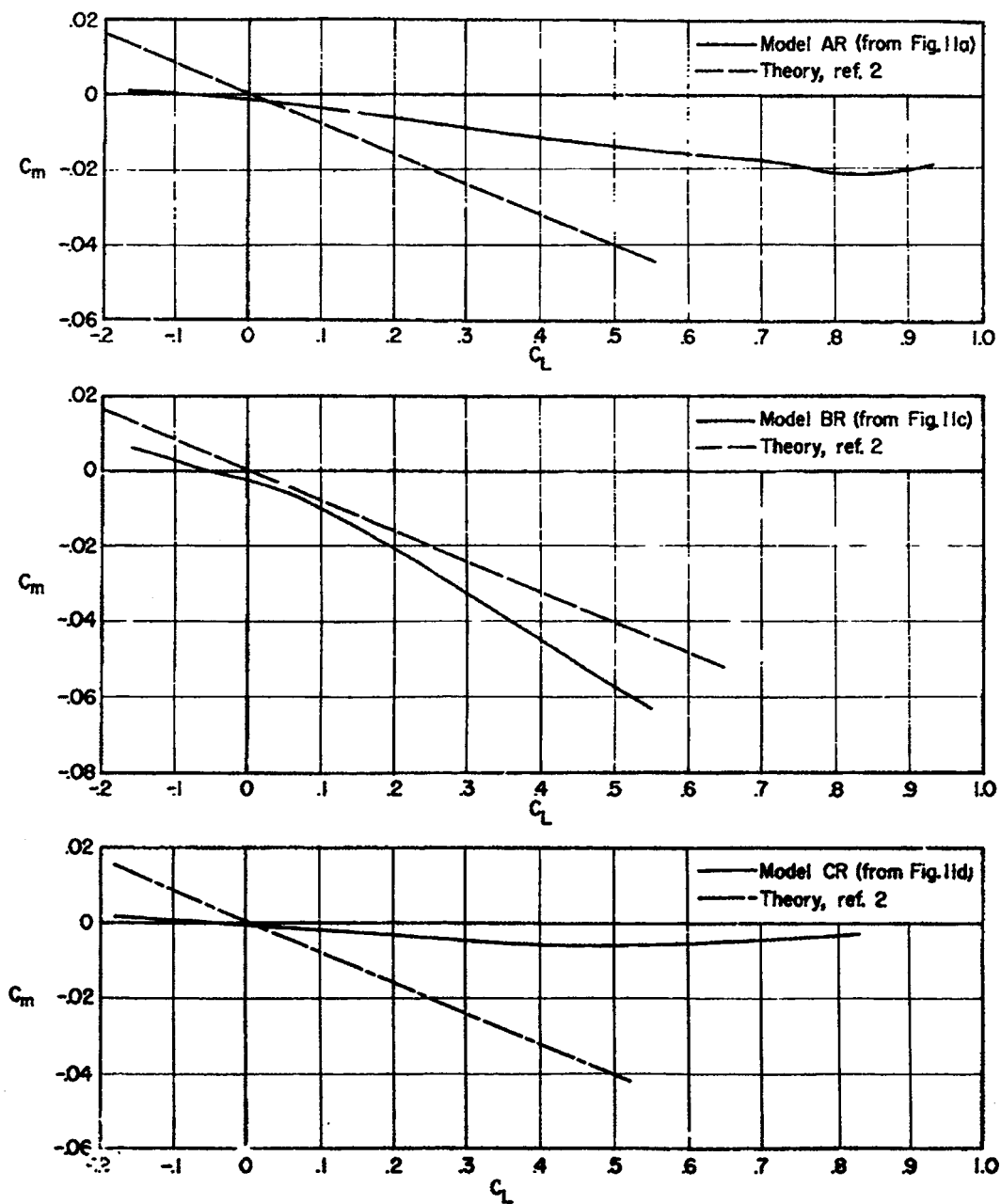
(e)  $M = 1.00$ .(f)  $M = 1.05$ .(g)  $M = 1.10$ .

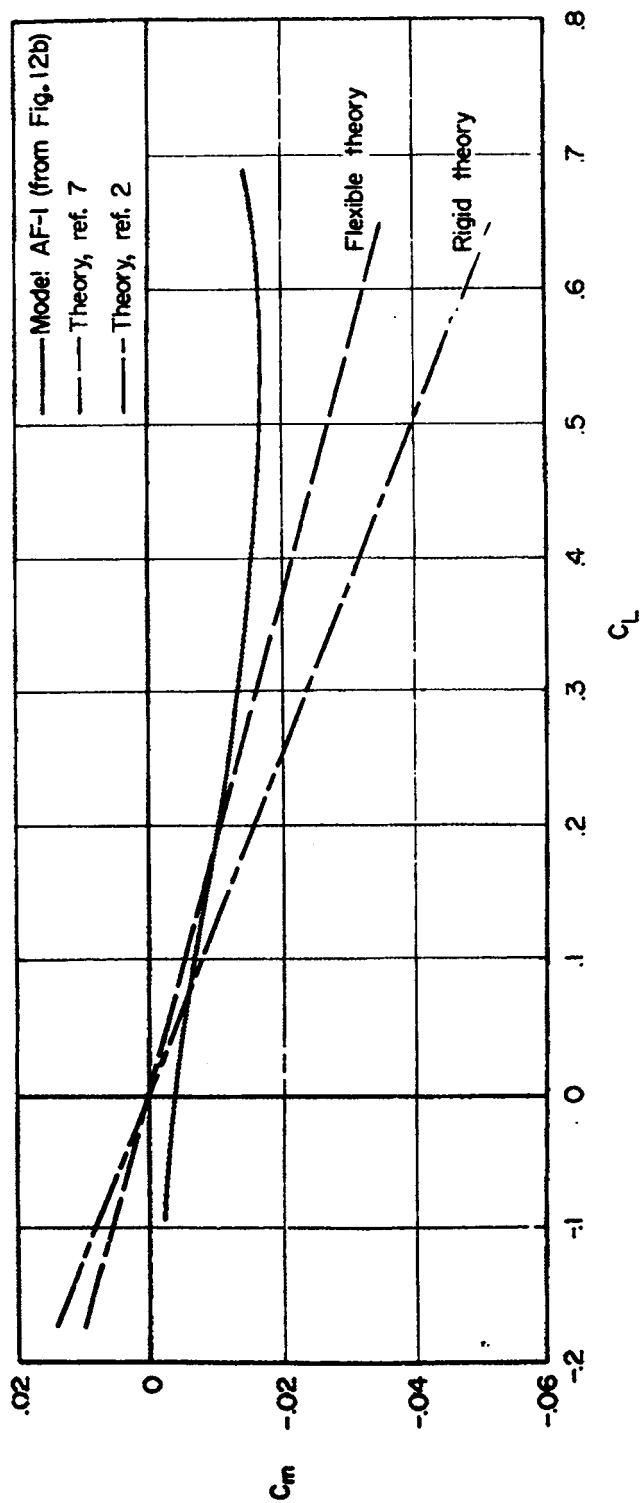
Figure 16.- Concluded.





(a) Rigid models.

Figure 17.- Comparison of experimental and calculated variations of pitching-moment coefficients with lift coefficient.  $M = 0.70$ ; Reynolds number per foot  $\approx 3.2 \times 10^6$ .



(b) Flexible Model AF-1.

Figure 17.- Concluded.

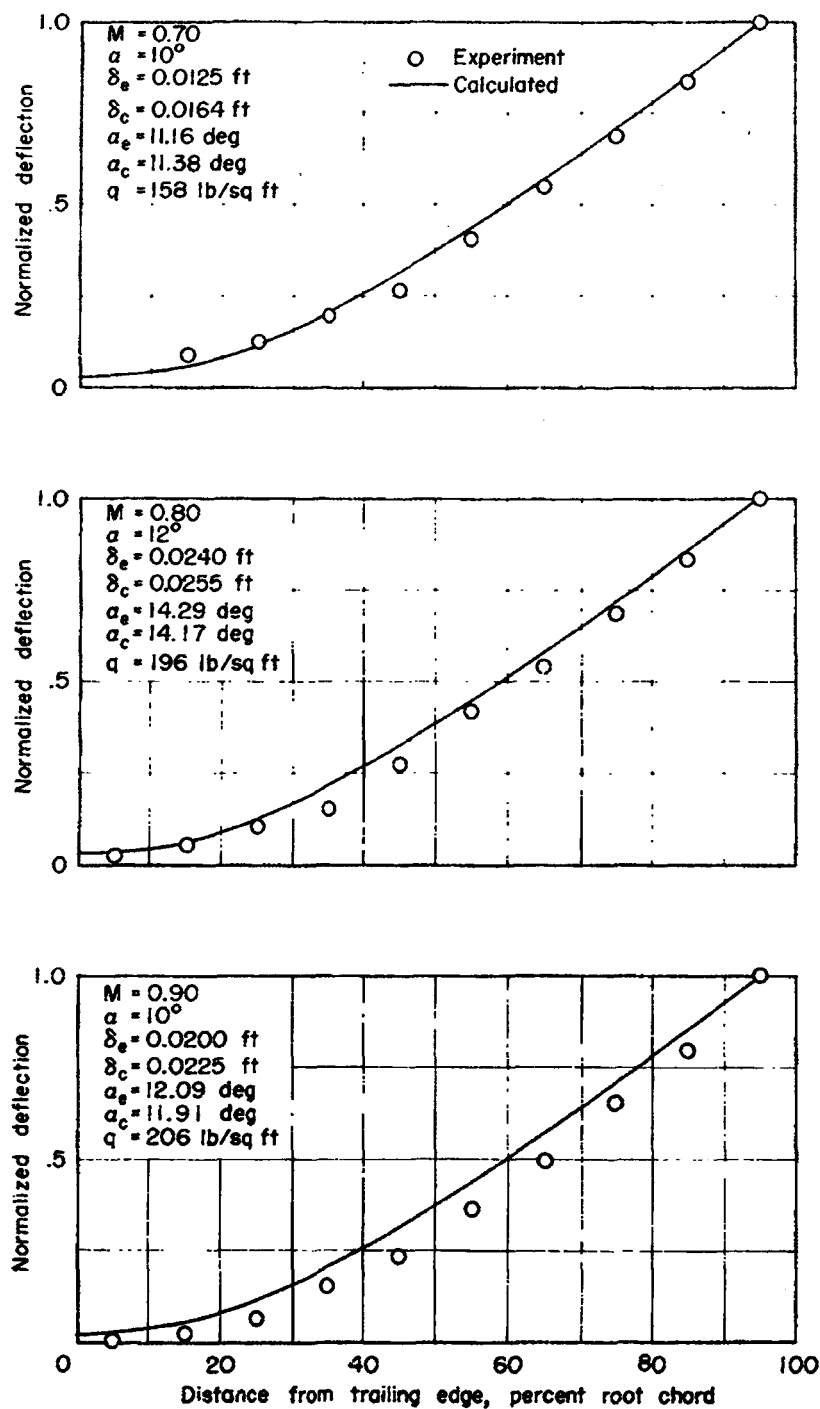


Figure 18.- Comparison of calculated and measured normalized deflection shapes for model AF-1. Reynolds number per foot  $\approx 3.2 \times 10^6$ .